Strange and charm quark contributions to the muon anomalous magnetic moment in lattice QCD with twisted-mass fermions

C. Alexandrou,[1,2] S. Bacchio,[2] A. De Santis,[3] A. Evangelista,[3] J. Finkenrath,[4] R. Frezzotti,[3] G. Gagliardi,[5] M. Garofalo,[6] N. Kalntis,[7] B. Kostrzewa,[8] V. Lubicz,[5] F. Pittler,[2] S. Romiti,[7] F. Sanfilippo,[9] S. Simula,[9] N. Tantalo,[3] C. Urbach,[6] and U. Wenger[7]

Extended Twisted Mass Collaboration

[1]*Department of Physics, University of Cyprus, 20537 Nicosia, Cyprus*
[2]*Computation-based Science and Technology Research Center, The Cyprus Institute, 20 Konstantinou Kavafi Street, 2121 Nicosia, Cyprus*
[3]*Dipartimento di Fisica and INFN, Università di Roma "Tor Vergata," Via della Ricerca Scientifica 1, I-00133 Roma, Italy*
[4]*Department of Theoretical Physics, European Organization for Nuclear Research, CERN, CH-1211 Genève 23, Switzerland*
[5]*Dipartimento di Matematica e Fisica, Università Roma Tre and INFN, Sezione di Roma Tre, Via della Vasca Navale 84, I-00146 Rome, Italy*
[6]*HISKP (Theory), Rheinische Friedrich-Wilhelms-Universität Bonn, Nussallee 14-16, 53115 Bonn, Germany*
[7]*Institute for Theoretical Physics, Albert Einstein Center for Fundamental Physics, University of Bern, Sidlerstrasse 5, CH-3012 Bern, Switzerland*
[8]*High Performance Computing and Analytics Lab, Rheinische Friedrich-Wilhelms-Universität Bonn, Friedrich-Hirzebruch-Allee 8, 53115 Bonn, Germany*
[9]*Istituto Nazionale di Fisica Nucleare, Sezione di Roma Tre, Via della Vasca Navale 84, I-00146 Rome, Italy*

(Received 4 December 2024; accepted 5 February 2025; published 4 March 2025)

We present a lattice calculation of the hadronic vacuum polarization (HVP) contribution of the strange and charm quarks to the anomalous magnetic moment of the muon in isospin symmetric QCD. We employ the gauge configurations generated by the Extended Twisted Mass Collaboration (ETMC) with $N_f = 2 + 1 + 1$ flavors of Wilson-clover twisted-mass quarks at five lattice spacings and at values of the quark mass parameters that are close and/or include the isospin symmetric QCD point of interest. After computing the small corrections necessary to precisely match this point, and carrying out an extrapolation to the continuum limit based on the data at lattice spacings $a \simeq 0.049$, 0.057, 0.068, 0.080 fm and spatial lattice sizes up to $L \simeq 7.6$ fm, we obtain $a_\mu^{\mathrm{HVP}}(s) = (53.57 \pm 0.63) \times 10^{-10}$ and $a_\mu^{\mathrm{HVP}}(c) = (14.56 \pm 0.13) \times 10^{-10}$, for the quark-connected strange and charm contributions, respectively. Our findings agree well with the corresponding results by other lattice groups.

DOI: 10.1103/PhysRevD.111.054502

I. INTRODUCTION

The polarization of the vacuum induced by fluctuations of a virtual photon into quarks and gluons, known as the hadronic vacuum polarization (HVP), has recently received a lot of attention and interest due to its importance in the Standard Model (SM) predictions of the anomalous magnetic moment of the muon a_μ. This quantity is currently investigated at the Fermi National Accelerator Laboratory (FNAL) [1] and at a forthcoming experiment at J-PARC (E34) [2]. The Fermilab Muon $g-2$ experiment (E989), has published the results of the analysis of the Run-1 data collected in 2018 [1,3–5], where a remarkably good agreement with the previous E821 measurement at BNL [6] is found. More recently, also the results of the analysis of the Run-2 and Run-3 data, collected in 2019 and 2020, have been published [7], with statistics increased by more than a factor of four and systematic errors reduced by more than a factor of two.

The current experimental world average [7] is $a_\mu^{\rm exp} = 116592059(22) \times 10^{-11}$ with a relative uncertainty of 0.19 ppm. The ongoing analysis of the remaining data from three additional years of data collection by the Fermilab Muon $g-2$ Collaboration is expected to lead to another factor of two of improvement in statistical precision, while a completely independent cross-check and possibly a further reduction of the total error will come from the forthcoming experiment planned at J-PARC.

From the theoretical side, the dominant source of uncertainty in the determination of a_μ comes from the HVP term at leading order in the electromagnetic (e.m.) coupling, $a_\mu^{\rm HVP}$ (see Ref. [8]). Presently, there are two approaches for obtaining precise predictions of the HVP contribution. The first one makes use of the experimental data on the process $e^+e^- \to$ hadrons, while the other one is represented by numerical simulations of QCD and QCD + QED on the lattice.

The data-driven determination of $a_\mu^{\rm HVP}$ quotes [8–10] a precision of approximately 0.6% and it corresponds to a SM prediction for a_μ that is found [7] to differ by about 5.0σ from the current experimental world average $a_\mu^{\rm exp}$. However, a recent determination of the cross section $e^+e^- \to \pi^+\pi^-(\gamma)$, carried out by the CMD-3 Collaboration [11], shows important tensions with previous measurements, including the one made by the CMD-2 Collaboration [12] and, if correct, would make nearly negligible the tension with $a_\mu^{\rm exp}$. Whether radiative corrections can provide an explanation for such tensions in the data-driven determination of $a_\mu^{\rm HVP}$ is presently under active investigation (see, e.g., Refs. [13–15] and also Ref. [16] for a first-principle isoQCD lattice calculation of the R-ratio smeared in Gaussian energy bins).

In recent years, impressive progress has been made by the lattice QCD community that enables the evaluation of $a_\mu^{\rm HVP}$ with increasing precision, reaching the goal of a few permille accuracy. A breakthrough concerning the precision achieved came from the lattice calculation performed by the BMW Collaboration in 2020 [17], corresponding to a relative uncertainty of 0.8%. This result has been recently updated by the same collaboration [18], by combining a refinement of their 2020 lattice computation with an experimental data-driven input for the very low energy tail of the R-ratio of the process $e^+e^- \to$ hadrons. In this hybrid approach, assuming that the e^+e^- experimental data of input have controlled systematics and are not affected by contributions of physics beyond the SM, they reach a precision of $\simeq 0.5\%$ and obtain a phenomenological prediction for $a_\mu^{\rm HVP}$ that, once combined with the SM computations for the QED and electroweak contributions to a_μ, yields a prediction for a_μ that deviates by only $\simeq 0.9\sigma$ from the current experimental value $a_\mu^{\rm exp}$. Moreover, very recently, the CLS/Mainz collaboration presented [19] its lattice prediction for $a_\mu^{\rm HVP}$ that has an accuracy of $\simeq 1\%$ ($\simeq 0.8\%$ for the isoQCD contribution) and that, once combined with the SM computations for the QED and electroweak contributions, is fully compatible within errors with $a_\mu^{\rm exp}$. The CLS/Mainz result exhibits a slightly larger central value than $a_\mu^{\rm exp}$ and is in small tension with the BMW 2020 result. Finally, also the RBC/UKQCD collaboration presented [20] a lattice result for the dominating light quark contribution to $a_\mu^{\rm HVP}$ that is in between the corresponding results of the CLS/Mainz and BMW collaborations and compatible with both of them within errors.

Furthermore, the BMW and the CLS/Mainz results are in strong tension (respectively $\simeq 2\sigma$ [17], $\simeq 4\sigma$ [18] and $\simeq 4\sigma$ [19]) with the data-driven one of Ref. [8] (i.e. without including the recent CMD3 data). Since 2020, i.e. after the appearance of Ref. [17], this issue has triggered a lot of investigations of the so-called window contributions to $a_\mu^{\rm HVP}$, which were first introduced by the RBC/UKQCD collaboration in Ref. [21]. Such quantities, obtained by introducing suitable weight functions in the Euclidean time-momentum representation of $a_\mu^{\rm HVP}$, have proven to be quite useful since at short and intermediate time distances they can be predicted with high accuracy on the lattice. In particular, in the so-called intermediate window the disagreement between $e^+e^- \to$ hadrons cross-section data-driven results, as quoted by Ref. [8] (i.e. without the recent CMD-3 result), and the lattice determinations has reached the remarkable level of $\simeq 4.5\sigma$ already in 2022 (see Ref. [22]). However, if one employs instead the recent determination of the cross section of $e^+e^- \to \pi^+\pi^-(\gamma)$ carried out by the CMD-3 collaboration [11], the experimental results for the intermediate window contribution to $a_\mu^{\rm HVP}$ are in agreement with the SM lattice prediction.

In this work, we present a high-precision determination of the quark-connected contributions to $a_\mu^{\rm HVP}$ due to strange and charm flavors that are obtained by the ETMC within the so-called isospin symmetric QCD (isoQCD), where isospin breaking effects, due to different up and down quark masses and quark electric charges, are neglected.

The analysis[1] is performed using the gauge configurations generated by ETMC [23–26] with $N_f = 2+1+1$ flavors of Wilson Clover twisted-mass sea quarks with masses tuned very close to the target isoQCD values, i.e. the ones corresponding to our scheme of choice for defining isoQCD which is the so-called Edinburgh/FLAG consensus [27,28]. We have computed the small nonperturbative corrections needed to fine-tune the bare

[1]We are presently working on the calculation of the dominating light-quarks quark-connected isoQCD contribution $a_\mu^{\rm HVP}(\ell)$ and, for that quantity, we have implemented a blinded analysis procedure whose details will be explained in a forthcoming publication. In the case of the contributions considered in this paper (as well as in the case of the isoQCD quark-disconnected and of the isospin breaking contributions on which we are also currently working) we have considered unnecessary to implement a blinded analysis.

TABLE I. ETMC gauge ensembles used to compute $a_\mu^{\rm HVP}(s)$ and $a_\mu^{\rm HVP}(c)$. The values of the lattice spacing and of the bare quark masses are fine-tuned to match our target definition of isoQCD, see Eq. (12), the one corresponding to the Edinburgh/FLAG consensus [27,28]. This is done by starting from the simulated gauge ensembles, listed in Table II, and by taking into account the reweighting factors needed to correct the small mistunings of the simulated bare parameters (see Appendices A and B).

Ensemble	V/a^4	$a^{\rm iso}$ [fm]	L [fm]	$am_\ell^{\rm iso}$	$am_s^{\rm iso}$	$am_c^{\rm iso}$	$am_{\rm cr}$
B64	$64^3 \times 128$	0.07948(11)	5.09	0.0006669(28)	0.018267(53)	0.23134(52)	−0.4138934(46)
B96	$96^3 \times 192$	0.07948(11)	7.63	0.0006669(28)	0.018267(53)	0.23134(52)	−0.4138934(46)
C80	$80^3 \times 160$	0.06819(14)	5.46	0.0005864(34)	0.016053(67)	0.19849(64)	−0.3964534(41)
C112	$112^3 \times 224$	0.06819(14)	7.64	0.0005864(34)	0.016053(67)	0.19849(64)	−0.3964534(41)
D96	$96^3 \times 192$	0.056850(90)	5.46	0.0004934(24)	0.013559(39)	0.16474(44)	−0.3761252(39)
E112	$112^3 \times 224$	0.04892(11)	5.48	0.0004306(23)	0.011787(55)	0.14154(54)	−0.3613136(75)

parameters to the target isoQCD values and, after applying these corrections to the simulated ensembles (listed in Table II in the Appendices), we obtain the corrected isoQCD physical-point ensembles listed in Table I, with lattice spacings $a \simeq 0.049$, 0.057, 0.068, 0.080 fm. Using these isoQCD physical-point ensembles, taking into account the tiny finite size effects (FSE) and adopting a proper Akaike-information-criterion (AIC)-based model average for the continuum limit extrapolation, the results that we obtain for the quark-connected strange and charm contributions to $a_\mu^{\rm HVP}$ are

$$a_\mu^{\rm HVP}(s) = (53.57 \pm 0.63) \times 10^{-10},$$
$$a_\mu^{\rm HVP}(c) = (14.56 \pm 0.13) \times 10^{-10}. \quad (1)$$

Here the quoted error is the total one resulting from purely statistical, mistuning corrections and continuum-limit extrapolation errors plus the tiny uncertainties related to FSE and to the finite current renormalization constant.

The results for partial short-distance (SD) window, intermediate window (W) and long distance (LD) window contributions are given in Sec. III. Our current results for SD and W window contributions are nicely consistent with, and supersede in accuracy, those we published in Ref. [22]. Compared to that paper, we now employ one physical-point ensemble at finer ($a \simeq 0.049$ fm) lattice spacing which allowed us to exclude the ensembles at unphysical values of the pion mass and at the coarsest lattice spacing used in Ref. [22] and to achieve a significant reduction of the statistical and continuum extrapolation errors. Furthermore, precisely because of this error reduction, we carried out a careful analysis of the small mistuning errors affecting our previous results, computed the required corrections and took into account the associated uncertainties, thus improving our control of the total errors.

The paper is organized as follows: In Sec. II, we provide the relevant notations and definitions. In Sec. III we present our determinations of the strange- and charm-quark connected contributions to the vector correlator, including a detailed analysis of the continuum limit. In Sec. IV, we conclude by presenting a comparison with other available lattice QCD calculations and an outlook.

Further technical information is given in the Appendices as follows: In Appendix A, we give details about our lattice setup and the bare parameters we used in Monte Carlo simulations, as a step "zero" in our definition of isoQCD. In Appendix B, we detail the procedure we apply to fine-tune the bare parameters of our lattice action in order to implement the chosen definition of isoQCD at a level of accuracy comparable with the statistical errors affecting the hadronic inputs used for theory renormalization. In Appendix C we discuss the evaluation of the strange and charm HVP [$a_\mu^{\rm HVP}(s)$ and $a_\mu^{\rm HVP}(c)$], along with the corresponding SD, LD and W, contributions precisely at the Edinburgh/FLAG isoQCD point determined in Appendix B. In Appendix D, we present technical details about our numerical estimate of the systematic effects on both the hadronic renormalization inputs (F_π, M_π, M_K, M_{D_s}) and $a_\mu^{\rm HVP}(s,c)$ themselves stemming from the small mistuning in the bare action parameters used in our Monte Carlo simulations. In Appendix E, we collect the values of the scale-invariant renormalization constants (RCs) of the vector and axial-vector local quark currents, Z_V and Z_A, employing the hadronic method of Ref. [22], which relies on Ward identities (WIs) and universality of renormalized matrix elements. Owing to a high statistics determination of the relevant correlators, we achieve a very precise determination of Z_V and Z_A, as needed to guarantee a few permille level statistical accuracy of the quark-connected strange and charm HVP terms at fixed lattice spacing.

II. TIME-MOMENTUM REPRESENTATION

Following our previous works [22,29–31], we adopt the time momentum representation [32] and, in continuum notation, evaluate the HVP contribution to the muon anomalous magnetic moment $a_\mu^{\rm HVP}$ as

$$a_\mu^{\rm HVP} = 2\alpha_{em}^2 \int_0^\infty dt t^2 K(m_\mu t) V(t), \quad (2)$$

where t is the Euclidean time and the kernel function $K(m_\mu t)$ is defined as[2]

$$K(z) = 2\int_0^1 dy(1-y)\left[1 - j_0^2\left(\frac{z}{2}\frac{y}{\sqrt{1-y}}\right)\right],$$
$$j_0(y) = \frac{\sin(y)}{y}. \tag{3}$$

The Euclidean vector correlator $V(t)$ is defined as

$$V(t) \equiv \frac{1}{3}\sum_{i=1,2,3}\int d^3x \langle J_i(\vec{x},t) J_i^\dagger(0)\rangle \tag{4}$$

with $J_i(x)$ being the e.m. current operator

$$J_i(x) \equiv \sum_{f=u,d,s,c,\ldots} J_i^f(x),$$
$$J_i^f(x) = q_{\mathrm{em},f}\bar{\psi}_f(x)\gamma_i\psi_f(x),$$
$$J_i(x) = -J_i^\dagger(x), \quad i = 1,2,3, \tag{5}$$

and $q_{\mathrm{em},f}$ the electric charge for the quark flavor f (in units of the positron charge).

The fermionic Wick contractions appearing in the right hand side (rhs) of Eq. (4) give rise to two distinct topologies of Feynman diagrams, namely to the quark-connected and quark-disconnected contributions. Connected contributions are flavor diagonal, while the disconnected ones have both diagonal and off-diagonal flavor components. In what follows we decompose a_μ^{HVP} into the following contributions

$$a_\mu^{\mathrm{HVP}} = a_\mu^{\mathrm{HVP}}(\ell) + a_\mu^{\mathrm{HVP}}(s) + a_\mu^{\mathrm{HVP}}(c) + a_\mu^{\mathrm{HVP}}(\mathrm{disc}) + \ldots, \tag{6}$$

where the first three terms correspond to the quark-connected contributions of mass degenerate up and down (ℓ) quarks, and a strange (s) and a charm (c) quark, respectively, while the fourth term represents all quark-disconnected (flavour diagonal and off-diagonal) contributions.[3] In Eq. (6) the ellipses corresponds to subleading terms, namely the isospin breaking effects and the contributions of quarks heavier than the charm in QCD + QED (i.e. the low energy effective theory of the Standard Model).

Following the suggestion of the RBC/UKQCD Collaboration [21], each of the terms appearing in Eq. (6) can further be decomposed by multiplying the integration kernel $K(m_\mu t)$ appearing in Eq. (2) with suitably smoothed Heaviside step-functions, namely

$$a_\mu^{\mathrm{HVP,w}} = 2\alpha_{em}^2\int_0^\infty dt\, t^2\, K(m_\mu t)\Theta^w(t)V(t)$$
$$w = \{\mathrm{SD}, \mathrm{W}, \mathrm{LD}\}, \tag{7}$$

where the time-modulating functions $\Theta^w(t)$ are given by

$$\Theta^{\mathrm{SD}}(t) \equiv 1 - \frac{1}{1+e^{-2(t-t_0)/\Delta}}, \tag{8}$$

$$\Theta^{\mathrm{W}}(t) \equiv \frac{1}{1+e^{-2(t-t_0)/\Delta}} - \frac{1}{1+e^{-2(t-t_1)/\Delta}}, \tag{9}$$

$$\Theta^{\mathrm{LD}}(t) \equiv \frac{1}{1+e^{-2(t-t_1)/\Delta}}, \tag{10}$$

with the parameters t_0, t_1, Δ chosen [21] to be equal to

$$t_0 = 0.4\ \mathrm{fm}, \quad t_1 = 1\ \mathrm{fm}, \quad \Delta = 0.15\ \mathrm{fm}. \tag{11}$$

The resulting time-modulating functions $\Theta^{\mathrm{SD,W,LD}}(t)$ are shown, e.g., in Fig. 1 of Ref. [22].

In this work, together with the full contributions $a_\mu^{\mathrm{HVP}}(s)$ and $a_\mu^{\mathrm{HVP}}(c)$, we also compute the three window observables, i.e. $a_\mu^{\mathrm{HVP,w}}$, $\mathrm{w} = \{\mathrm{SD}, \mathrm{W}, \mathrm{LD}\}$, for the strange and charm (connected) HVP terms. Our results are presented and discussed in the next section.

The light quark-connected contribution, $a_\mu^{\mathrm{HVP}}(\ell)$, and all quark-disconnnected contributions, $a_\mu^{\mathrm{HVP}}(\mathrm{disc})$, which also include those arising from the product of two strange/charm e.m. currents, will be given in a forthcoming paper devoted to the full HVP contribution a_μ^{HVP} within isoQCD, Ref. [33]. In a subsequent paper the leading isospin breaking effects on a_μ^{HVP} in QCD + QED with u, d, s and c active flavours will be included too [34].

III. THE CONNECTED CONTRIBUTIONS TO $a_\mu^{\mathrm{HVP}}(s)$ AND $a_\mu^{\mathrm{HVP}}(c)$

In this section we present our numerical results for $a_\mu^{\mathrm{HVP}}(f)$, where $f = \{s, c\}$, and for the corresponding window quantities. The results presented here improve and supersede in accuracy the ones previously obtained in Ref. [22].

With respect to our previous calculation, in addition to the first five $N_f = 2+1+1$ isoQCD ensembles listed in Table I (with lattice spacings $a \simeq \{0.079, 0.068, 0.057\}$ fm) we included an additional ensemble, the entry E112 in the

[2]The leptonic kernel $K(z)$ is proportional to z^2 at small values of z and it approaches 1 as $z \to \infty$.

[3]Following Ref. [22], the separation of quark connected and disconnected contributions to a given correlator can be expressed in terms of local correlators by formally introducing, when needed, a suitable number of extra valence flavors (having the same masses as the physical quarks) and the corresponding ghosts. The different flavor contributions to a_μ^{HVP}, appearing in Eq. (6), can be separately extracted from local current-current vector correlators computed within the renormalizable mixed action lattice setup described in detail in Appendix A of Ref. [22], which is briefly recalled also in Appendix A of this work.

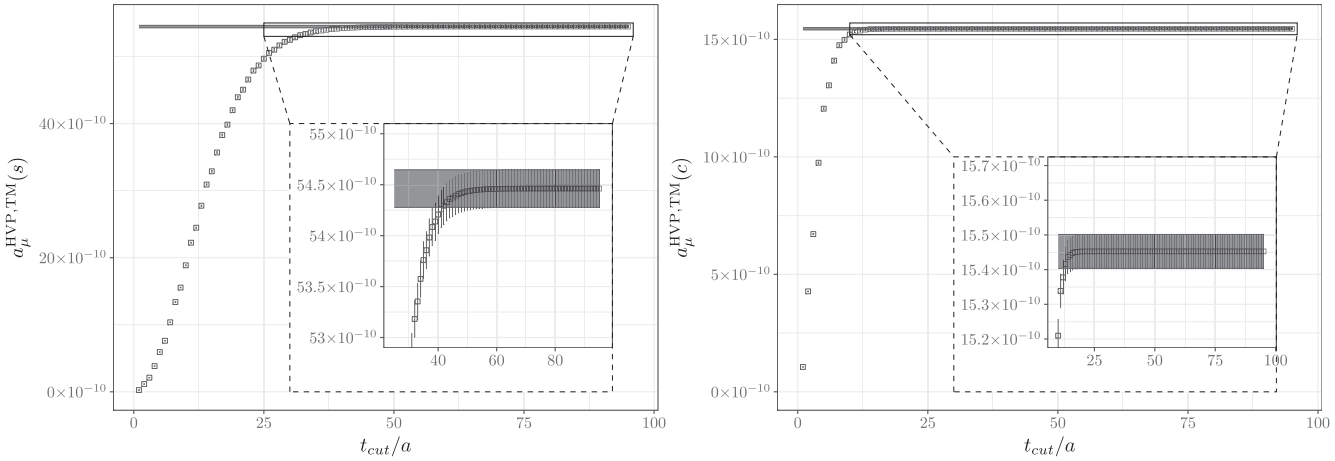

FIG. 1. The left-panel shows $a_\mu^{\mathrm{HVP}}(s)$ while the right-panel shows $a_\mu^{\mathrm{HVP}}(c)$ as functions of t_{cut}. The data correspond to the ensemble D96, to the TM regularization and to the smallest simulated values of the valence strange and charm masses. A detailed study of the dependence upon the valence and see quark masses is presented in the Appendices C and D. We observe that the results are independent of t_{cut}/a within the statistical errors for large enough t_{cut}/a. Similar plots can be shown for the other simulated values of the lattice spacing, of the valence masses and for the OS regularization.

same table, with the finest lattice spacing ($a \simeq 0.049$ fm) ever simulated by the ETMC. This allowed us to better control the continuum extrapolations and, consequently, to reduce the corresponding systematic errors. Moreover, to further improve the accuracy of our results, in this work we computed the corrections needed to fine-tune the bare parameters of our simulations in order to precisely match our target definition of isoQCD, the Edinburgh/FLAG consensus [27,28], corresponding to the following hadronic inputs

$$M_\pi^{\mathrm{iso}} = 135.0\,\mathrm{MeV}, \quad M_K^{\mathrm{iso}} = 494.6\,\mathrm{MeV},$$
$$M_{D_s}^{\mathrm{iso}} = 1967\,\mathrm{MeV}, \quad F_\pi^{\mathrm{iso}} = 130.5\,\mathrm{MeV}. \tag{12}$$

The numerical procedure that we used to compute these corrections, on both the input observables and on the target quantities $a_\mu^{\mathrm{HVP}}(f)$, is described in the Appendices A–D to which we refer for all the technical details of our lattice setup and of our calculation. Here below we present our results by focusing on the main steps of the analysis, i.e. the extraction of the observables from the lattice correlators, the estimate of FSE and the continuum extrapolations.

We consider two lattice discretizations of the e.m. currents $J_f^{\mu,\mathrm{reg}}$ in Eq. (5), with reg $= \{\mathrm{TM}, \mathrm{OS}\}$, corresponding to the so-called twisted-mass (TM) and Osterwalder-Seiler (OS) regularizations [see Eqs. (B30) and (B31)] and compute the corresponding connected Wick contractions of the vector correlators $V_f^{\mathrm{reg}}(t)$ [see Eq. (4)] on each gauge ensemble. The two regularizations share a universal continuum limit and differ at fixed cutoff by $O(a^2)$ lattice artifacts (see the final part of Appendix B). From the lattice correlators $V_f^{\mathrm{reg}}(t)$ we extracted $a_\mu^{\mathrm{HVP,reg}}(f)$ by using the following discretized version of Eq. (2),

$$a_\mu^{\mathrm{HVP,reg}}(f; an_{\mathrm{min}}) = 2\alpha_{\mathrm{em}}^2 \lim_{t_{\mathrm{cut}}\mapsto\infty} a^3 \times \sum_{n=n_{\mathrm{min}}}^{t_{\mathrm{cut}}/a} w(n) n^2 K(m_\mu an) V_f^{\mathrm{reg}}(an),$$
$$a_\mu^{\mathrm{HVP,reg}}(f) \equiv a_\mu^{\mathrm{HVP,reg}}(f;0). \tag{13}$$

In Eq. (13), $n = t/a$ is the Euclidean time in lattice units and the lattice spacing a is intended to be fixed at $a = a^{\mathrm{iso}}$. We restrict the integral appearing in Eq. (2) to the region $[t_{\mathrm{min}}, t_{\mathrm{cut}}]$, indicate explicitly the limit $t_{\mathrm{cut}} \mapsto \infty$ and keep track of the dependence upon $t_{\mathrm{min}} = an_{\mathrm{min}}$ to better control our continuum extrapolations (see below). By setting the weights $w(n)$ to $3/8$ at the endpoints, to $3/4$ when $n - n_{\mathrm{min}}$ is a multiple of 3 and to $9/8$ for the remaining points (Simpson-3/8 rule), our discretization differs from the corresponding integral by errors of $O(a^2)$.

As customary, we take the $t_{\mathrm{cut}} \mapsto \infty$ limit of our results by performing a plateaux-analysis of the partial sums as functions of t_{cut}. Examples of these analyses are shown in Fig. 1.

In order to quantify the FSE on $a_\mu^{\mathrm{HVP,reg}}(f)$ we perform simulations on two different volumes. More precisely, among the ensembles listed in Table I, the B64 and the B96 have the same value of the lattice spacing, $a \simeq 0.08$ fm, but different physical volumes, $L \sim 5.1$ fm and $L' \sim 7.6$ fm. Similarly, the lattice spacing of the ensembles C80 and C112 is $a \simeq 0.07$ fm and the corresponding linear sizes are $L \sim 5.4$ fm and $L' \sim 7.6$ fm. Figure 2 shows the ratio of $a_\mu^{\mathrm{HVP,reg}}(f)$ computed on the two systems of different linear size (and volume). As it can be seen, the FSE on $a_\mu^{\mathrm{HVP,reg}}(f)$ are totally negligible with respect to the statistical errors. Nevertheless, we use these

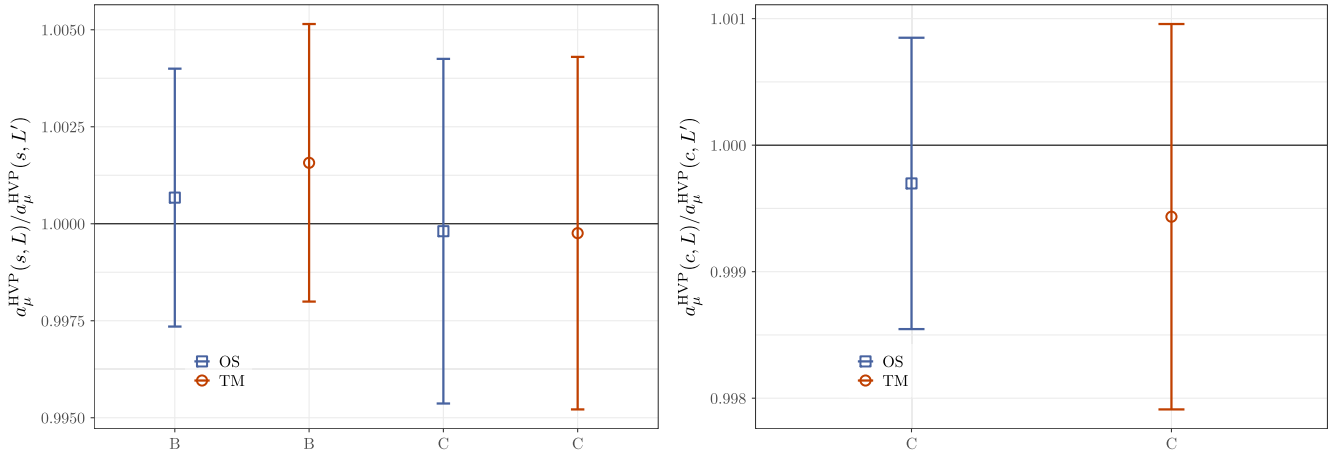

FIG. 2. Ratio of $a_\mu^{\rm HVP}(s)$ left and $a_\mu^{\rm HVP}(c)$ for the two regularizations OS and TM, computed at the lattice spacing $a \simeq 0.07$ fm with two linear sizes $L \sim 5.4$ fm and $L' \sim 7.6$ fm using the ensembles C80 and C112. For the strange contribution we plot also the same ratio at $a = 0.08$ fm with two linear sizes $L \sim 5.1$ fm and $L' \sim 7.6$ fm using the ensembles B64 and B96.

results to estimate a systematic error associated with FSE as in [16] according to the formula

$$\Delta_{\rm FSE}(f) = \max_{{\rm reg},a}\left\{|a_\mu^{\rm HVP,reg}(f,L) - a_\mu^{\rm HVP,reg}(f,L')|{\rm erf} \times \left(\frac{|a_\mu^{\rm HVP,reg}(f,L) - a_\mu^{\rm HVP,reg}(f,L')|}{\sqrt{2}\sqrt{\Delta^{\rm reg}(f,L)^2 + \Delta^{\rm reg}(f,L')^2}}\right)\right\}, \quad (14)$$

where the maximum is computed over the two regularization and over the lattice spacings $a \simeq 0.07$ fm and $a \simeq 0.08$ fm when available. $\Delta^{\rm reg}(f,L)$ is the statistical error of $a_\mu^{\rm HVP,reg}(f,L)$ and erf is the error function.

By keeping track of the dependence of our results upon $t_{\rm min}$ in Eq. (13) we are able to better control our continuum extrapolations and to safely estimate the associated systematic errors. To this end we perform two different analyses. In the main branch of the analysis we fix $t_{\rm min} = 0$ and perform the continuum extrapolations of our results at fixed cutoff that in this case, with a small abuse of notation, we simply call $a_\mu^{\rm HVP,reg}(f)$. In the second branch of the analysis we keep $t_{\rm min}$ fixed in physical units by interpolating the results $a_\mu^{\rm HVP,reg}(f; an_{\rm min})$ as functions of the integer variable $n_{\rm min}$. Then we extrapolate the results $a_\mu^{\rm HVP,reg}(f;t_{\rm min})$ to the continuum and add the contributions of the region $[0, t_{\rm min}]$ of the integral appearing in Eq. (2). These are computed at NNLO in continuum perturbation theory by using the RHAD [35] software package using the pole mass value for the quarks. Finally we study the dependence upon $t_{\rm min}$ of the results thus obtained to better quantify the systematic errors associated with our continuum extrapolations. In the case of the full and SD contributions and in both branches of the analysis we compute the tree-level $O(a^2)$ cutoff effects on our results in lattice perturbation theory and remove them before performing the continuum extrapolations as described in detail in [22].

We will provide numerical evidence of the branch of the analysis in which we keep track of the dependence upon $t_{\rm min}$ in the case of the SD contributions $a_\mu^{\rm HVP,SD}(f)$ which are most sensitive to cutoff effects (see Sec. III A). To extrapolate $a_\mu^{\rm HVP}(f) \equiv a_\mu^{\rm HVP,reg}(f;t_{\rm min}=0)$ to the continuum limit we consider the following ansatz,

$$a_\mu^{\rm HVP,reg}(f) = P_0 + P_1^{\rm reg}a^2 + P_2^{\rm reg}a^4, \quad (15)$$

for both the regularizations. We also explore fits in which we remove $P_2^{\rm TM}$ and $P_2^{\rm OS}$ either together or separately and fits in which the a^4 term is replaced with $a^2/[\log(a^2/\lambda_0^2)]^n$ for $n = 1, 2, 3$ and $\lambda_0 = 1$ fm. The analogous terms with $n < 0$ are removed by subtraction of tree level lattice artifacts as detailed in Sec. III A of [22]. We perform all the above fits for three different datasets: (1) the full dataset available, (2) the dataset excluding the coarsest lattice spacing in both regularizations or only in one of them, and (3) the dataset excluding the next-to-coarsest lattice spacing in both regularizations or only in one of them.

To find the average over the different results of the analyses of the lattice data, we make use of the procedure developed in Ref. [36]. Namely, starting from N computations with mean values x_k and uncertainties σ_k $(k = 1, \ldots, N)$, based on the same set of input data, their average x and uncertainty σ_x are given by

$$x = \sum_{k=1}^{N}\omega_k x_k, \quad \sigma_x^2 = \sigma_{x,\rm stat}^2 + \sigma_{x,\rm syst}^2,$$
$$\sigma_{x,\rm stat}^2 = \sum_{k=1}^{N}\omega_k\sigma_k^2, \quad \sigma_{x,\rm syst}^2 = \sum_{k=1}^{N}\omega_k(x_k - x)^2, \quad (16)$$

where ω_k represents the weight associated with the kth determination. The weights ω_k are based on the Bayesian

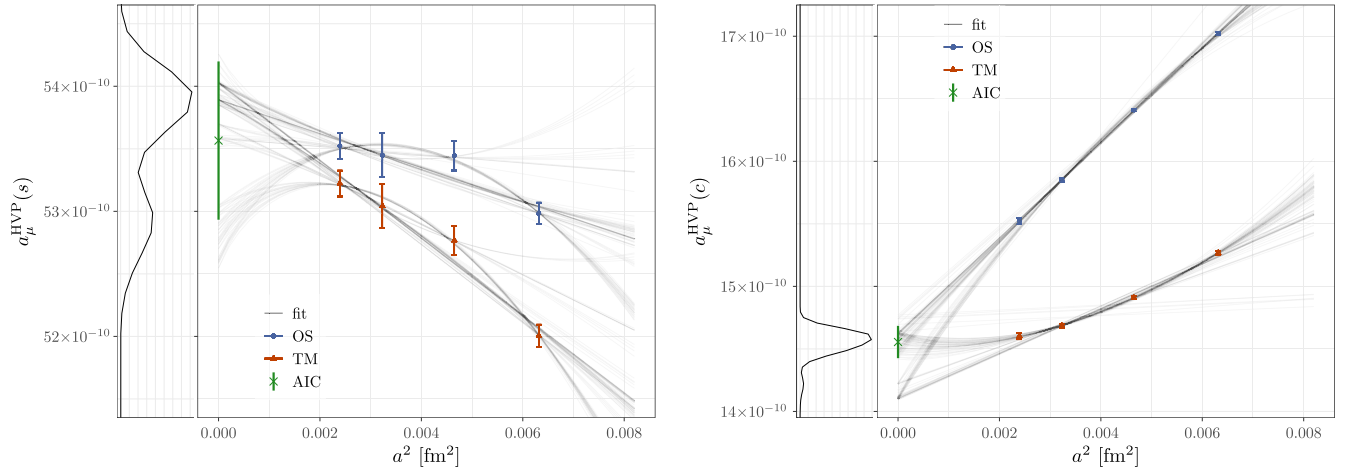

FIG. 3. Continuum extrapolation of the full $a_\mu^{\rm HVP}$ for the strange (left panel) and charm (right panel). For each panel, we show the OS lattice regularization as blue circles, the TM regularization in red triangles, the gray lines represent the various fits, the BAIC average of the continuum values is plotted as a green cross and on the left we show the histogram of the continuum values weighted according to the BAIC.

Akaike information criterion (BAIC) [37], namely

$$\omega_k \propto \exp[-(\chi^2_k + 2N_{\rm parms} - 2N_{\rm data})/2], \tag{17}$$

where χ^2_k is the value of the χ^2 variable for the kth computation, $N_{\rm parms}$ is the number of free parameters and $N_{\rm data}$ the number of data points.[4] We show the resulting fits in Fig. 3. The final results, obtained after averaging all the results of the different analyses by using Eq. (16), are

$$\begin{aligned} a_\mu^{\rm HVP}(s) &= 53.57(41)_{\rm stat}(48)_{\rm cont}(3)_{\rm FSE} \times 10^{-10} \\ &= 53.57(63) \times 10^{-10}, \end{aligned} \tag{18}$$

$$\begin{aligned} a_\mu^{\rm HVP}(c) &= 14.56(10)_{\rm stat}(9)_{\rm cont}(0)_{\rm FSE} \times 10^{-10} \\ &= 14.56(13) \times 10^{-10}, \end{aligned} \tag{19}$$

where $(.)_{\rm stat}$ represents the statistical error resulting from the continuum extrapolation, computed as $\sigma_{x,\rm stat}$ from Eq. (16), $(.)_{\rm cont}$ denotes the systematic error due to the continuum limit, calculated as $\sigma_{x,\rm syst}$ from Eq. (16) and $(.)_{\rm FSE}$ denotes the error associated with the finite volume of our lattice simulations, which is calculated using Eq. (14). All the errors are summed in quadrature to give the total error.

The results for each window contribution are presented in the next subsections.

[4]We have verified that the use of the original Akaike information criterion (AIC) proposed in Ref. [38], namely $\omega_k \propto e^{-(\chi^2_k + 2N_{\rm parms} - N_{\rm data})/2}$ leads to very similar averages and errors as compared with those corresponding to the use of Eq. (17).

A. The short-distance window contributions $a_\mu^{\rm HVP,SD}(s)$ and $a_\mu^{\rm HVP,SD}(c)$

The SD window contribution is obtained by inserting the kernel $\Theta^{\rm SD}(t)$ of Eq. (8) in the sum of Eq. (13). As for the full contribution, we take the $t_{\rm cut} \mapsto \infty$ limit of our results performing a plateaux-analysis of the partial sums as functions of $t_{\rm cut}$. Then we subtract from our results the tree-level $O(a^2)$ cutoff effects calculated in lattice perturbation theory (the details of the tree-level calculation can be found in Appendix E of Ref. [22]). We first discuss the first branch of our analysis, i.e. taking first $t_{\rm min} = 0$. The continuum limit and the uncertainty estimate are addressed using the same strategy used in the full contribution. In Fig. 4 we show the continuum extrapolations and the resulting values are

$$\begin{aligned} a_\mu^{\rm HVP,SD}(s) &= 9.063(16)_{\rm stat}(22)_{\rm cont}(1)_{\rm FSE} \times 10^{-10} \\ &= 9.063(27) \times 10^{-10}, \end{aligned} \tag{20}$$

$$\begin{aligned} a_\mu^{\rm HVP,SD}(c) &= 11.61(7)_{\rm stat}(11)_{\rm cont}(0)_{\rm FSE} \times 10^{-10} \\ &= 11.61(14) \times 10^{-10}. \end{aligned} \tag{21}$$

The different contributions to the error are estimated as for the full $a_\mu^{\rm HVP}$ above. Our previous determination in Ref. [22] was $a_\mu^{\rm HVP,SD}(s) = 9.074(64) \times 10^{-10}$ and $a_\mu^{\rm HVP,SD}(c) = 11.61(27) \times 10^{-10}$. The values given here are compatible with our previous determination and they exhibit a significant reduction of the error.

We now compare the main analysis above to our second branch, i.e. the one when we keep $t_{\rm min}$ fixed in physical units by interpolating the results $a_\mu^{\rm HVP,SD}(f; an_{\rm min})$ as functions of the integer variable $n_{\rm min}$. We then extrapolate

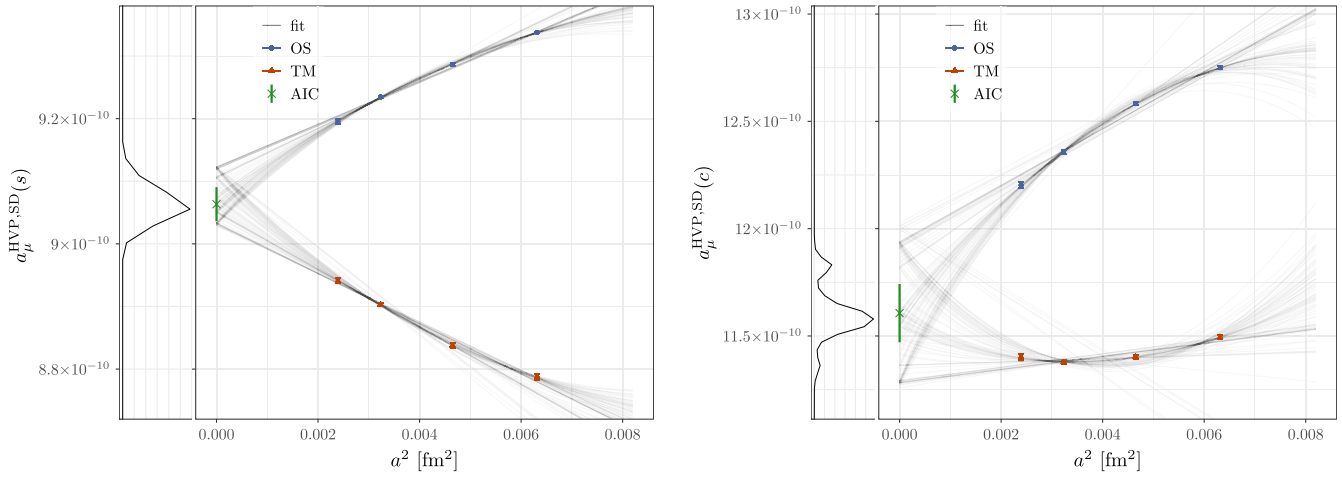

FIG. 4. Continuum extrapolation of the short distance contribution to a_μ^{HVP} for the strange (left panel) and charm (right panel). For each panel, we show the OS lattice regularization as blue circles, the TM regularization in red triangles, the gray lines represent the various fits, the BAIC average of the continuum values is plotted as a green cross and on the left we show the histogram of the continuum values weighted according to the BAIC.

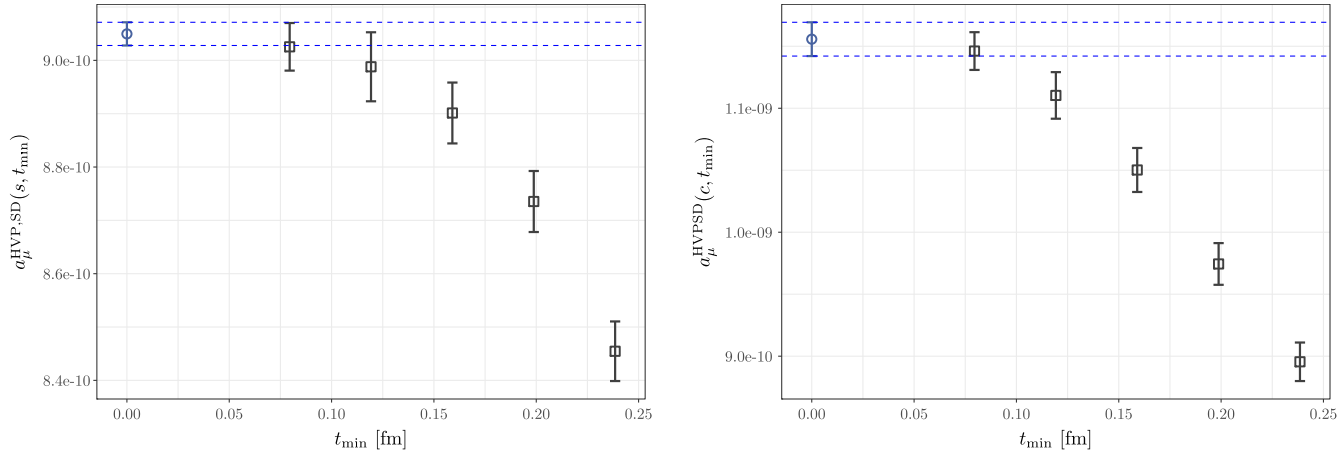

FIG. 5. Continuum values of the short distance contribution to $a_\mu^{\mathrm{HVP,SD}}$ computed as a function of t_{min} for the strange (left panel) and charm (right panel). The blue point is computed with the first branch of our analysis, i.e. setting $t_{\mathrm{min}} = 0$ while the black points are computed with the second branch, i.e. keeping t_{min} fixed in physical units and adding the contribution in the region $[0, t_{\mathrm{min}}]$ that we have computed at NNLO in continuum perturbation theory by using the RHAD [35] software package using the pole mass value for the quarks.

those values to the continuum with the same strategy as in the first analysis branch and then add to the integral appearing in Eq. (2) the contribution from the region $[0, t_{\mathrm{min}}]$, which we compute at NNLO in continuum perturbation theory by using the RHAD [35] software package. For evaluating this perturbative contribution we use the renormalized pole mass for the charm quarks and a very conservative energy threshold in the Laplace transform (connecting the R-ratio to the Euclidean correlator), i.e. $E_{\mathrm{min}} = 1.8$ GeV for the strange and $E_{\mathrm{min}} = 3.9$ GeV for the charm. With these energy thresholds we verify that the results do not change within error if instead the $\overline{\mathrm{MS}}$ quark mass is employed. The results obtained from both branches of our analysis are plotted in Fig. 5. We observe that for small enough t_{min} the two branches of our analysis give compatible results, corroborating the result obtained with the first branch.

B. The intermediate windows $a_\mu^{\mathrm{HVP,W}}(s)$ and $a_\mu^{\mathrm{HVP,W}}(c)$

The intermediate window contribution is obtained by inserting the kernel $\Theta^{\mathrm{W}}(t)$ of Eq. (9) in the sum of Eq. (13). As for the full contribution, we take the $t_{\mathrm{cut}} \mapsto \infty$ limit of our results performing a plateaux-analysis of the partial sums as functions of t_{cut}. The continuum extrapolation is done as in the case of the full contributions and the various fits are shown in Fig. 6. The values obtained are

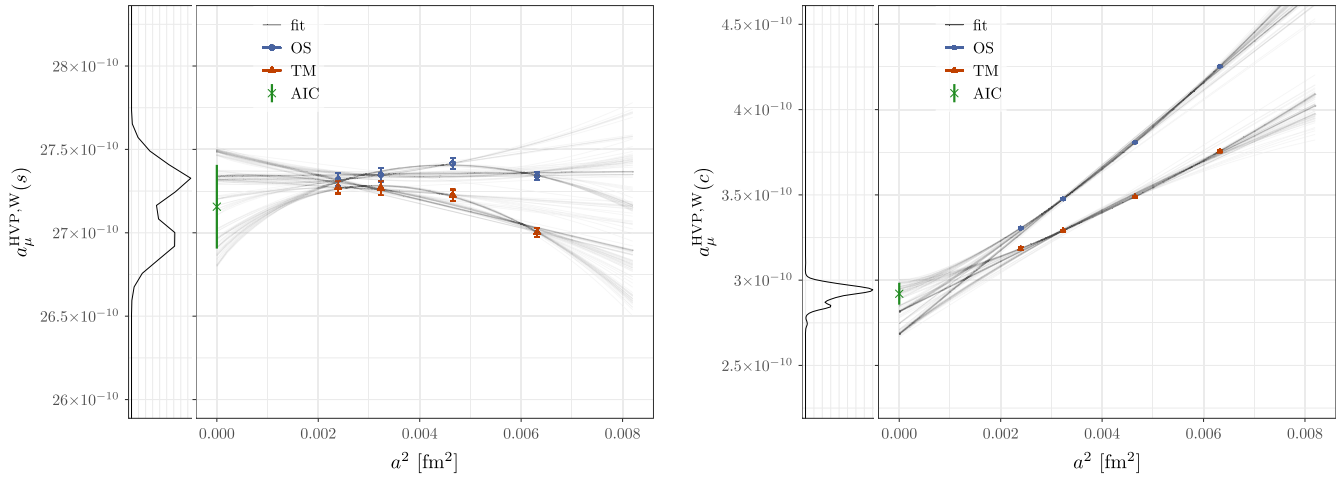

FIG. 6. Continuum extrapolation of the intermediate window contribution to $a_\mu^{\mathrm{HVP,W}}$ for the strange (left panel) and charm (right panel). For each panel, we show the OS lattice regularization as blue circles, the TM regularization in red triangles, the gray lines represent the various fits, the BAIC average of the continuum values is plotted as a green cross and on the left we show the histogram of the continuum values weighted according to the BAIC.

$$a_\mu^{\mathrm{HVP,W}}(s) = 27.16(15)_{\mathrm{stat}}(20)_{\mathrm{cont}}(2)_{\mathrm{FSE}} \times 10^{-10} = 27.16(25) \times 10^{-10}, \quad (22)$$

$$a_\mu^{\mathrm{HVP,W}}(c) = 2.920(43)_{\mathrm{stat}}(48)_{\mathrm{cont}}(0)_{\mathrm{FSE}} \times 10^{-10} = 2.920(64) \times 10^{-10}. \quad (23)$$

Our previous determination in Ref. [22] was $a_\mu^{\mathrm{HVP,W}}(s) = 27.28(20) \times 10^{-10}$ and $a_\mu^{\mathrm{HVP,W}}(c) = 2.90(12) \times 10^{-10}$. The values given here are compatible with our previous determination. We note a reduction of the error for the charm contribution only. For the strange contribution the total error slightly increased with respect to our previous determination. This is due to the contribution to the statistical errors coming from the uncertainties on the fine-tuning corrections that at this level of precision, must be taken into account (see Appendix D and, in particular, Fig. 18). Indeed in Ref. [22] only the dominant bare parameters fine-tuning effects were considered, namely those coming from valence quark masses and the light quark sea mass.

C. The long distance windows $a_\mu^{\mathrm{HVP,LD}}(s)$ and $a_\mu^{\mathrm{HVP,LD}}(c)$

The long-distance window contribution is computed by inserting the kernel $\Theta^{\mathrm{LD}}(t)$ from Eq. (10) into the summation of Eq. (13). As for the full contribution, we take the $t_{\mathrm{cut}} \mapsto \infty$ limit of our results performing a plateaux-analysis of the partial sums as functions of t_{cut}. The continuum extrapolation is done as in the case of the full contributions and the values obtained are

$$a_\mu^{\mathrm{HVP,LD}}(s) = 17.32(29)_{\mathrm{stat}}(24)_{\mathrm{cont}}(1)_{\mathrm{FSE}} \times 10^{-10} = 17.32(38) \times 10^{-10}, \quad (24)$$

$$a_\mu^{\mathrm{HVP,LD}}(c) = 0.01352(37)_{\mathrm{stat}}(68)_{\mathrm{cont}}(14)_{\mathrm{FSE}} \times 10^{-10} = 0.01352(79) \times 10^{-10}. \quad (25)$$

By subtracting the values in the continuum of the short distance, Eq. (21), and of the intermediate window, Eq. (23), from the full contribution, Eq. (19), and by propagating the error in quadrature we get $a_\mu^{\mathrm{HVP,LD}}(s) = 17.35(73) \times 10^{-10}$ and $a_\mu^{\mathrm{HVP,LD}}(c) = 0.03(20) \times 10^{-10}$, which are consistent with Eq. (25) but with larger errors.

IV. COMPARISON WITH OTHER LATTICE QCD RESULTS AND OUTLOOK

In the isospin symmetric limit of QCD, according to the Edinburgh/FLAG consensus as specified in Eq. (12), we obtain results for the total, short-distance, intermediate window and long-distance contributions to a_μ^{HVP} coming from the strange and charm quark-connected diagrams that are listed in Eqs. (18)–(25). In Figs. 7 and 8, to the best of our knowledge, we compare[5] our results in this work with the corresponding ones by other lattice studies, see Refs. [8,17–19,21,22,29,39–47].

[5]The comparison of our results with the other lattice determinations presented in Figs. 7 and 8 has been done by directly using the results quoted in Refs. [8,17–19,21,22,29,39–47] without taking into account the small differences associated with the fact that, in some cases, slightly different definitions of isoQCD have been adopted. Moreover, the BMW-24 [18] results correspond to the window [0.2.8] fm, obtained by setting $t_0 = 2.8$ fm in Eq. (8).

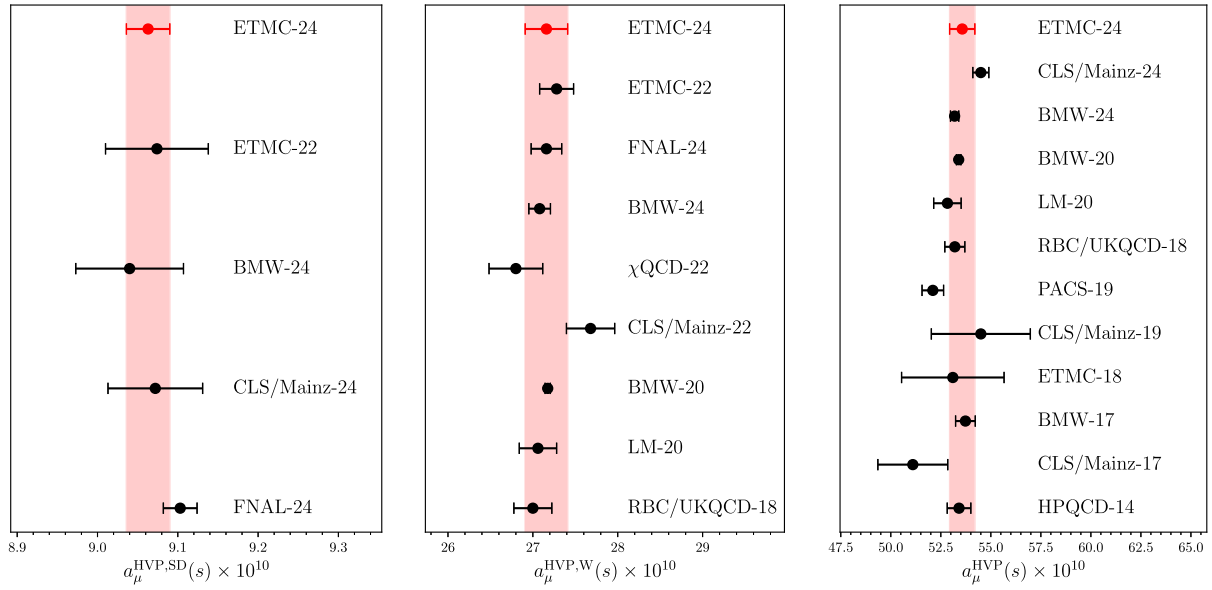

FIG. 7. We show the lattice QCD determinations of $a_\mu^{\mathrm{HVP,SD}}(s)$ (left panel), of $a_\mu^{\mathrm{HVP,W}}(s)$ (central panel) and of $a_\mu^{\mathrm{HVP}}(s)$ (right panel) obtained in this work (in red) and in Refs. [17–19,21,22,29,39–48]. In all panels the vertical red band corresponds to our determination and it is displayed to ease the comparison. Note that the BMW-24 result of Ref. [18] for $a_\mu^{\mathrm{HVP}}(s)$ refers to a time window defined in the range [0, 2.8] fm.

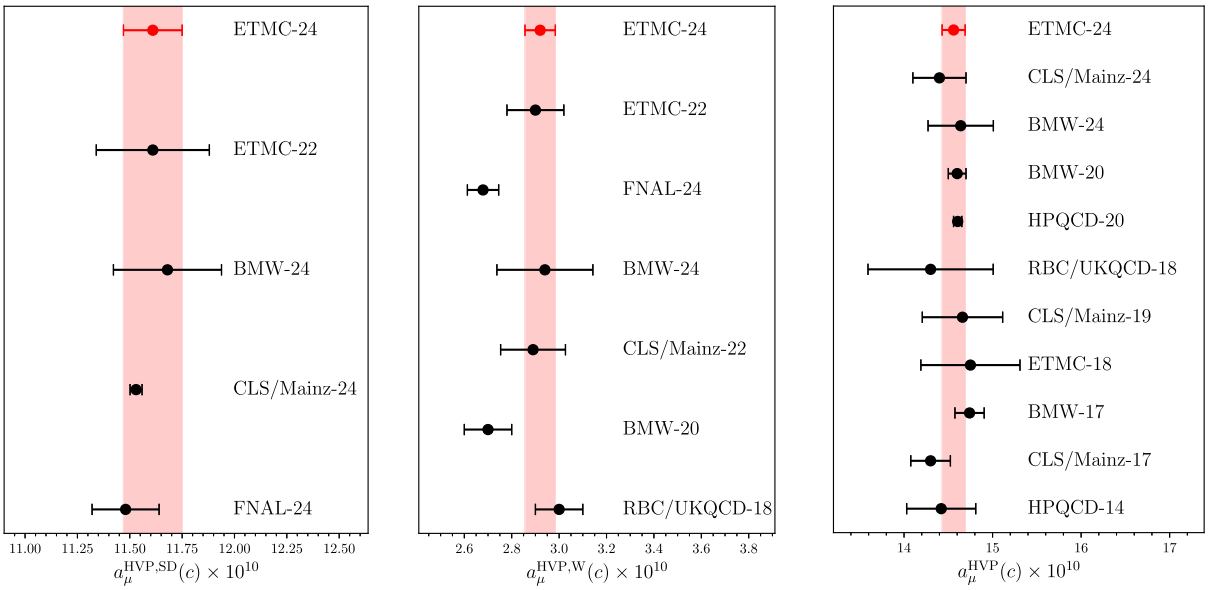

FIG. 8. We show the lattice QCD determinations of $a_\mu^{\mathrm{HVP,SD}}(c)$ (left panel), of $a_\mu^{\mathrm{HVP,W}}(c)$ (central panel) and of $a_\mu^{\mathrm{HVP}}(c)$ (right panel) obtained in this work (in red) and in Refs. [17–19,21,22,29,39–49]. In all panels the vertical red band corresponds to our determination and it is displayed to ease the comparison. Note that the BMW-24 result of Ref. [18] for $a_\mu^{\mathrm{HVP}}(c)$ refers to a time window defined in the range [0, 2.8] fm.

The results for the short-distance and intermediate window contributions to $a_\mu^{\mathrm{HVP}}(s)$ and $a_\mu^{\mathrm{HVP}}(c)$ presented in this work exhibit in most cases a significant reduction of the uncertainty compared to our previous determination in Ref. [22]. This is more notable in the case of $a_\mu^{\mathrm{HVP,SD}}(c)$ as it can be appreciated in the left panel of Fig. 8. Our new determinations of $a_\mu^{\mathrm{HVP,SD}}(s)$ and $a_\mu^{\mathrm{HVP,W}}(c)$ are presently the most precise among the available lattice results.

In addition to this update, we also provide the total and the long-distance quark-connected contributions for $a_\mu^{\mathrm{HVP}}(s)$ and $a_\mu^{\mathrm{HVP}}(c)$, see Eqs. (18), (19), (24), and (25). Our results for the total quark-connected $a_\mu^{\mathrm{HVP}}(s)$ and

$a_\mu^{\mathrm{HVP}}(c)$ are in excellent agreement with all the other lattice determinations. The result we quote for $a_\mu^{\mathrm{HVP}}(c)$ is among the most accurate ones.

Being concerned with analyses that give results with typical total errors at the 0.5–1.0% level, we have chosen a definite prescription for the isosymmetric QCD theory, the Edinburgh/FLAG consensus, and made an effort to consider and quantify as well as possible all the uncertainties related to the necessary hadronic renormalization inputs and their feedback on the observables of interest here. The subpercent accuracy level achieved for the observable estimators at finite lattice spacing has required considering a set of continuum fit ansatz that go well beyond the basic fit linear in a^2 and are averaged using the AIC, as discussed in Sec. III. A similar kind of analyses will likely be necessary for several other physical observables that are obtained in lattice studies at comparable accuracy level.

At the level of precision reached now for $a_\mu^{\mathrm{HVP}}(s)$ and $a_\mu^{\mathrm{HVP}}(c)$ and their partial window contributions, the evaluation of the leading isospin breaking contributions within QCD + QED with u, d, s and c active flavours is of course mandatory. This work is currently in progress by our collaboration using the RM123 method [50]. Similarly in progress is the evaluation of the light quark-connected contribution, $a_\mu^{\mathrm{HVP}}(\ell)$, and the all-flavours quark-disconnected contribution, $a_\mu^{\mathrm{HVP}}(\mathrm{disc})$, as well as of the corresponding leading isospin breaking corrections in QCD + QED. The open-source packages tmLQCD [51–54], Lemon [55], DD-αAMG [56–59], QPhiX [60,61] and QUDA [62–64] have been used in the ensemble generation.

ACKNOWLEDGMENTS

We thank all members of ETMC for the most enjoyable collaboration. We thank Giancarlo Rossi for a careful reading of the draft of this paper. C. A. acknowledges partial support from the European Joint Doctorate AQTIVATE that received funding from the European Union's research and innovation programme under the Marie Sklodowska-Curie Doctoral Networks action under the Grant Agreement No. 101072344 and from the European Union's Horizon 2020 Research and Innovation Programme ENGAGE under the Marie Sklodowska-Curie COFUND scheme with grant agreement No. 101034267. N. K., S. R., and U. W. acknowledge support by the Swiss National Science Foundation (SNSF) Project No. 200020_208222. V. L., F. S., G. G., R. F., N. T., A. E., and A. D. S. are supported by the Italian Ministry of University and Research (MUR) under the Grant No. PNRR-M4C2-I1.1-PRIN 2022-PE2 nonperturbative aspects of fundamental interactions, in the Standard Model and beyond F53D23001480006 funded by E. U.-NextGenerationEU. S. B., J. F., and F. P. received financial support from the Inno4scale project, which received funding from the European High-Performance Computing Joint Undertaking (JU) under Grant Agreement No. 101118139. The JU receives support from the European Union's Horizon Europe Programme. J. F. received support by the DFG research unit FOR5269 "Future methods for studying confined gluons in QCD" and acknowledges financial support by the Next Generation Triggers project [65]. M. G. and C. U. are supported by the Deutsche Forschungsgemeinschaft (DFG, German Research Foundation) as part of the CRC 1639 NuMeriQS—Project No. 511713970. F. S. is supported by ICSC—Centro Nazionale di Ricerca in High Performance Computing, Big Data and Quantum Computing, funded by European Union-NextGenerationEU and by Italian Ministry of University and Research (MUR) projects FIS_00001556 and PRIN_2022N4W8WR. The authors gratefully acknowledge the Gauss Centre for Supercomputing e.V. [66] for funding this project by providing computing time on the GCS Supercomputers SuperMUC-NG at Leibniz Supercomputing Centre and JUWELS [67,68] at Juelich Supercomputing Centre. The authors acknowledge the Texas Advanced Computing Center (TACC) at The University of Texas at Austin for providing HPC resources (Project ID PHY21001). The authors gratefully acknowledge PRACE for awarding access to HAWK at Höchstleistungsrechenzentrum Stuttgart (HLRS) within the project with Id Acid 4886. We acknowledge the Swiss National Supercomputing Centre (CSCS) and the EuroHPC Joint Undertaking for awarding this project access to the LUMI supercomputer, owned by the EuroHPC Joint Undertaking, hosted by CSC (Finland) and the LUMI consortium through the Chronos programme under project IDs CH17-CSCS-CYP and CH21-CSCS-UNIBE as well as the EuroHPC Regular Access Mode under project ID EHPC-REG-2021R0095. We are grateful to CINECA and EuroHPC JU for awarding this project access to Leonardo supercomputing facilities hosted at CINECA. We gratefully acknowledge EuroHPC JU for the computer time on Leonardo-Booster provided to us through the Extreme Scale Access Call grant EHPC-EXT-2024E01-027. We gratefully acknowledge CINECA for the provision of GPU time under the specific initiative INFN-LQCD123 and IscrB S-EPIC.

DATA AVAILABILITY

The data that support the findings of this article are not publicly available upon publication because it is not technically feasible and/or the cost of preparing, depositing, and hosting the data would be prohibitive within the terms of this research project. The data are available from the authors upon reasonable request.

APPENDIX A: LATTICE SETUP AND SIMULATION DETAILS

In this work, we compute correlation functions, and from these extract the physical observables of interest, on the gauge ensembles produced by ETMC in isoQCD with $N_f = 2+1+1$ flavors of Wilson-Clover twisted-mass quarks as described in Refs. [23–26]. As already done in Ref. [22], the correlation functions are evaluated in the mixed-action lattice theory corresponding to the following renormalizable action

$$S = S_{\rm YM}(g_0) + S_{\rm TM}(\mu_i^{\rm sim}, m_{\rm cr}^{\rm sim}) + S_{\rm ghost}(m_f^{\rm sim}, m_{\rm cr}^{\rm sim}) + S_{\rm OS}(m_f, m_{\rm cr}). \tag{A1}$$

The gluon action is the mean-field improved Iwasaki one [69],

$$S_{\rm YM}(g_0) = \frac{\beta}{3}\sum_x\sum_{\mu<\nu}(b_0\{1-{\rm ReTr}[U_{\mu\nu}^{1\times1}(x)]\} + b_1\{1-{\rm ReTr}[U_{\mu\nu}^{1\times2}(x)]\}), \tag{A2}$$

where $\beta = 6/g_0^2$ is the inverse bare QCD gauge coupling, $b_1 = -0.331$, $b_0 = 1\text{–}8b_1$, $U_{\mu\nu}^{1\times1}(x)$ is the square plaquette and $U_{\mu\nu}^{1\times2}(x)$ the rectangular one, see Ref. [70].

The twisted-mass (TM) quark action depends on the bare mass parameters $\mu_i^{\rm sim}$ with $i = \{\ell, \sigma, \delta\}$ and on the critical mass $m_{\rm cr}^{\rm sim}$ and is given by

$$\begin{aligned} S_{\rm TM}(\mu_i^{\rm sim}, m_{\rm cr}^{\rm sim}) = &\sum_x \bar\Psi_\ell\{\gamma_\mu\overline{\nabla}_\mu[U] - i\tau^3\gamma_5(W^{\rm cl}[U] + m_{\rm cr}^{\rm sim}) \\ &+ \mu_\ell^{\rm sim}\}\Psi_\ell \\ &+ \sum_x \bar\Psi_h\{\gamma_\mu\overline{\nabla}_\mu[U] - i\tau^1\gamma_5(W^{\rm cl}[U] \\ &+ m_{\rm cr}^{\rm sim}) + \mu_\sigma^{\rm sim} + \tau^3\mu_\delta^{\rm sim}\}\Psi_h, \end{aligned} \tag{A3}$$

where $\Psi_\ell^T = (u, d)$ is the light-quark TM doublet, $\Psi_h^T = (c, s)$ is the heavy TM doublet. We refer to Ref. [71] for the explicit expression of the Wilson-Clover term $W^{\rm cl}[U]$. The TM quark action is nondiagonal in the charm-strange flavor sector.

The Osterwalder-Seiler (OS) action is flavor-diagonal also in the heavy sector and is given by

$$S_{\rm OS}(m_f, m_{\rm cr}) = \sum_f\sum_x \bar q_f\{\gamma_\mu\overline{\nabla}_\mu[U] - ir_f\gamma_5(W^{\rm cl}[U] + m_{\rm cr}) + m_f\}q_f, \tag{A4}$$

where the flavor index $f = \{u, d, s, c\}$ runs over the four lightest quarks and, in isoQCD, we take $m_u = m_d = m_\ell$ and set $r_{u,c} = 1$ and $r_{d,s} = -1$. In the rhs of Eq. (A4) it is assumed that $|r_f| = 1$ and $m_{\rm cr} \equiv m_{\rm cr}(g_0^2; r_f)|_{r_f=+1}$.

Finally, we have the *ghost* action, which is given by

$$\begin{aligned} S_{\rm ghost}(m_f^{\rm sim}, m_{\rm cr}^{\rm sim}) = &\sum_f\sum_x \bar\phi_f\{\gamma_\mu\overline{\nabla}_\mu[U] \\ &- ir_f\gamma_5(W^{\rm cl}[U] + m_{\rm cr}^{\rm sim}) + m_f^{\rm sim}\}\phi_f, \end{aligned} \tag{A5}$$

where the pseudoquarks ϕ_f are the bosonic fields associated with the OS quark fields q_f and, therefore, in this case we set $r_{u,c} = 1$ and $r_{d,s} = -1$.

By integrating out all the quarks and pseudoquarks fields appearing in S, one gets the weight that should be used to generate the gluon field gauge configurations corresponding to the action given in Eq. (A1). This, up to its normalization, is given by

$$P[U] = e^{-S_{\rm YM}(g_0)} \times \mathcal{D}_{\rm TM}^{\ell}(\mu_\ell^{\rm sim}, m_{\rm cr}^{\rm sim})\mathcal{D}_{\rm TM}^{h}(\mu_\sigma^{\rm sim}, \mu_\delta^{\rm sim}, m_{\rm cr}^{\rm sim}) \times \prod_f \frac{\mathcal{D}_{\rm OS}^f(m_f, m_{\rm cr})}{\mathcal{D}_{\rm OS}^f(m_f^{\rm sim}, m_{\rm cr}^{\rm sim})} \tag{A6}$$

$$= e^{-S_{\rm YM}(g_0)} \times \frac{\mathcal{D}_{\rm TM}^{h}(\mu_\sigma^{\rm sim}, \mu_\delta^{\rm sim}, m_{\rm cr}^{\rm sim})}{\mathcal{D}_{\rm OS}^s(m_s^{\rm sim}, m_{\rm cr}^{\rm sim})\,\mathcal{D}_{\rm OS}^c(m_c^{\rm sim}, m_{\rm cr}^{\rm sim})} \times \prod_f \mathcal{D}_{\rm OS}^f(m_f, m_{\rm cr}), \tag{A7}$$

where

$$\begin{aligned} \mathcal{D}_{\rm TM}^{h}(\mu_\sigma^{\rm sim}, \mu_\delta^{\rm sim}, m_{\rm cr}^{\rm sim}) &= {\rm det}\{\gamma_\mu\overline{\nabla}_\mu[U] - i\tau^1\gamma_5(W^{\rm cl}[U] + m_{\rm cr}^{\rm sim}) + \mu_\sigma^{\rm sim} + \tau^3\mu_\delta^{\rm sim}\}, \\ \mathcal{D}_{\rm OS}^f(m_f^{\rm sim}, m_{\rm cr}^{\rm sim}) &= {\rm det}\{\gamma_\mu\overline{\nabla}_\mu[U] - ir_f\gamma_5(W^{\rm cl}[U] + m_{\rm cr}^{\rm sim}) + m_f^{\rm sim}\}, \end{aligned} \tag{A8}$$

and where, in passing from Eqs. (A6) to (A7), we use the relation

$$\begin{aligned} \mathcal{D}_{\rm TM}^{\ell}(\mu_\ell^{\rm sim}, m_{\rm cr}^{\rm sim}) &= {\rm det}\{\gamma_\mu\overline{\nabla}_\mu[U] - i\tau^3\gamma_5(W^{\rm cl}[U] + m_{\rm cr}^{\rm sim}) + \mu_\ell^{\rm sim}\} \\ &= \mathcal{D}_{\rm OS}^u(\mu_\ell^{\rm sim}, m_{\rm cr}^{\rm sim})\,\mathcal{D}_{\rm OS}^d(\mu_\ell^{\rm sim}, m_{\rm cr}^{\rm sim}). \end{aligned} \tag{A9}$$

Some important remarks are in order. Our gluon gauge field configurations are generated with the action $S_{\rm YM}(g_0) + S_{\rm TM}(\mu_i^{\rm sim}, m_{\rm cr}^{\rm sim})$ which, at the price of introducing charm-strange flavor mixing at fixed cutoff, is automatically $\mathcal{O}(a)$-improved. In addition, it has a real and positive weight, which can thus be interpreted as a probability density and which is given by

$$P^{\rm sim}[U] = e^{-S_{\rm YM}(g_0)} \times \mathcal{D}^{\ell}_{\rm TM}(\mu^{\rm sim}_{\ell}, m^{\rm sim}_{\rm cr}) \mathcal{D}^{h}_{\rm TM}(\mu^{\rm sim}_{\sigma}, \mu^{\rm sim}_{\delta}, m^{\rm sim}_{\rm cr}). \tag{A10}$$

The OS quarks and the corresponding ghosts are introduced in our setup for two reasons:

(i) to avoid the technical complications associated with the heavy-flavor mixing at finite cutoff in the calculation of physical observables which we define in terms of the OS quarks: this is possible because the TM and OS actions can be matched by relying on the following, renormalization scale and scheme independent, relations

$$m_{\ell} = \mu_{\ell}, \quad m_s = \mu_{\sigma} - \frac{Z_P}{Z_S}\mu_{\delta}, \quad m_c = \mu_{\sigma} + \frac{Z_P}{Z_S}\mu_{\delta}, \tag{A11}$$

and/or matching physical quantities computed with both the TM and OS actions (see below). Once the matching is performed, the ratio of the TM and the ghost determinants appearing in Eq. (A7) differs from unit by a mere lattice artifact of $O(a^2)$,

$$\frac{\mathcal{D}^{h}_{\rm TM}(\mu^{\rm sim}_{\sigma}, \mu^{\rm sim}_{\delta}, m^{\rm sim}_{\rm cr})}{\mathcal{D}^{s}_{\rm OS}(m^{\rm sim}_{s}, m^{\rm sim}_{\rm cr})\, \mathcal{D}^{c}_{\rm OS}(m^{\rm sim}_{c}, m^{\rm sim}_{\rm cr})} = 1 + O(a^2). \tag{A12}$$

This implies that our mixed-action lattice theory, which is fully unitary in the light-quarks sector, can also be considered unitary in the heavy-quarks sector up to tiny $O(a^2)$ violations;

(ii) to improve the precision of the tuning of the critical mass counterterm $m_{\rm cr}$ and to match our target definition of isoQCD by fine-tuning the OS quark masses at the values $m_f = m_f^{\rm iso}$: this is accomplished by evaluating the reweighting factors appearing in Eq. (A6),

$$W_f(m_f, m_{\rm cr}) = \frac{\mathcal{D}^{f}_{\rm OS}(m_f, m_{\rm cr})}{\mathcal{D}^{f}_{\rm OS}(m^{\rm sim}_{f}, m^{\rm sim}_{\rm cr})}, \tag{A13}$$

which are identically equal to one when $m_f = m_f^{\rm sim}$ and $m_{\rm cr} = m_{\rm cr}^{\rm sim}$.

In the remaining part of this appendix, we explain how the simulated values of the bare parameters $\mu_i^{\rm sim}$ and $m_{\rm cr}^{\rm sim}$ are fixed during the Monte Carlo simulations. The fine-tuning of the bare parameters, i.e. the determination of the parameters $m_f^{\rm iso}$ and $m_{\rm cr}$, will be the subject of Appendix B.

The critical mass counterterm $m_{\rm cr}^{\rm sim} \sim 1/a$ is set to a unique value for all flavors [72] and is tuned, at each simulated value of the bare gauge coupling g_0, in order to guarantee automatic $\mathcal{O}(a)$-improvement of physical observables [73,74]. This is done, as explained in detail in Ref. [23], by computing the so-called partially conserved axial current (PCAC) *untwisted* quark mass of the TM light doublet,

$$2m_{\rm PCAC}(m^{\rm sim}_f, m_{\rm cr}) = \frac{\sum_{\vec{x}} \langle [\partial_0 \bar{\chi}_{\ell} \gamma_5 \gamma_0 \tau^1 \chi_{\ell}](t,\vec{x}) [\bar{\chi}_{\ell} \gamma_5 \tau^1 \chi_{\ell}](0) \rangle}{\sum_{\vec{x}} \langle [\bar{\chi}_{\ell} \gamma_5 \gamma_0 \tau^1 \chi_{\ell}](t,\vec{x}) [\bar{\chi}_{\ell} \gamma_5 \gamma_0 \tau^1 \chi_{\ell}](0) \rangle} \tag{A14}$$

$$\chi_{\ell}(x) = \exp\left(-i\frac{\pi}{4}\gamma_5\tau^3\right)\Psi_{\ell}(x),$$
$$\bar{\chi}_{\ell}(x) = \bar{\Psi}_{\ell}(x)\exp\left(-i\frac{\pi}{4}\gamma_5\tau^3\right), \tag{A15}$$

and by determining a value of $m_{\rm cr} = m_{\rm cr}^{\rm sim}$ such that the condition $|a m_{\rm PCAC}(m^{\rm sim}_f, m^{\rm sim}_{\rm cr})| < 0.1 a m^{\rm sim}_{\ell}/Z_A$ is well fulfilled. Here $m^{\rm sim}_{\ell} = \mu^{\rm sim}_{\ell}$ is the bare mass of the light TM doublet and Z_A is an estimate, for which even a modest accuracy of several percents is enough, of the renormalization constant of the operator $\bar{\chi}_{\ell}\gamma_5\gamma_0\tau^1\chi_{\ell}$.

In the early stages of the Monte Carlo simulations of the various ensembles, at each $\beta = 6/g_0^2$, the value of $m^{\rm sim}_{\ell}$ is chosen so as to obtain M_{π} as close as possible to the reference value $M_{\pi} = 135$ MeV. The simulated values of $\mu^{\rm sim}_{\sigma}$ and $\mu^{\rm sim}_{\delta}$, i.e. the bare mass parameters of the heavy TM doublet, are tuned in order to reproduce the renormalization group invariant (RGI) values $M_{D_s}/f_{D_s} = 7.9(0.1)$ and $m^{\rm sim}_c/m^{\rm sim}_s = 11.8(0.2)$. As detailed in Ref. [23], the two conditions above are first imposed on the mass parameters m_s and m_c of the valence quark action (A.4), for some trial values of the sea quark mass parameters μ_{σ} and μ_{δ}. We then use Eq. (A.11) to set $\mu_{\sigma} = \frac{1}{2}(m_s + m_c)$ while μ_{δ} is determined by the equivalent to Eq. (A11), but statistically more precise condition of matching the mass of the unitary Kaon, i.e. the mass obtained from the two-point correlators with interpolating operators $\bar{\Psi}_{\ell}\gamma_5\Psi_h$ and $\bar{\Psi}_h\gamma_5\Psi_{\ell}$, which is made out of the fields entering in the TM action, to the mass of the valence kaon evaluated using the OS quark lattice action with $r_s = -r_u$. Note that by following this strategy the renormalization scale and scheme independent ratio Z_P/Z_S appearing in Eq. (A11) is not needed. After this matching step, the Monte Carlo simulation is then repeated at the selected values of μ_{σ} and μ_{δ} and a set of corresponding gauge configurations is used to determine again m_s and m_c from the conditions $M_{D_s}/f_{D_s} = 7.9(0.1)$ and $m^{\rm sim}_c/m^{\rm sim}_s = 11.8(0.2)$. After convergence of this iterative procedure we get the values of $m^{\rm sim}_s$ and $m^{\rm sim}_c$ as well as of $\mu^{\rm sim}_{\sigma}$ and $\mu^{\rm sim}_{\delta}$.

The essential information on the ETMC ensembles that are relevant for this work are collected in Table II. With respect to Ref. [22] two new dedicated gauge ensembles, the cE211.044.112 and the cC211.060.112, are included in the current analysis to improve the control of cutoff and

TABLE II. We provide the full list of the ETMC gauge ensembles used in this work. These are produced by performing Monte Carlo simulations with the action $S_{\rm YM}(g_0) + S_{\rm TM}(\mu_i^{\rm sim}, m_{\rm cr}^{\rm sim})$ and, therefore, with the probabilistic weight $P^{\rm sim}[U]$ given in Eq. (A10), see Refs. [23–26]. The bare parameters of these simulations (reported in the table) are slightly different from the ones (determined in this work) corresponding to our target definition of isoQCD which, among the other inputs, prescribes $M_\pi^{\rm iso} = 135$ MeV. The ensembles at heavier pion masses, listed in the last six lines of the table, are only used to check the determination of the fine-tuned isoQCD bare parameters [see Eq. (B22) and the related discussion]. The large volumes ensembles with $M_\pi \simeq M_\pi^{\rm iso}$, listed in the first six lines of the table, are corrected for the small mistunings of the bare parameters by applying the reweighting technique thoroughly discussed in Appendix B. The values of the light, strange and charm quark masses corresponding to our definition of isoQCD ($m_{\ell,s,c}^{\rm iso}$), along with the values of the critical mass counterterm ($m_{\rm cr}$) and the lattice spacing $a^{\rm iso}$, which we use for the present calculation of the strange and charm HVP, are reported in Table I. Note the different naming conventions used in Table I to distinguish the reweighted ensembles from the simulated ones that are listed here.

Ensemble	β	V/a^4	$a^{\rm sim}$ (fm)	$a\mu_\ell^{\rm sim}$	M_π (MeV)	$M_\pi L$
cB211.072.64	1.778	$64^3 \times 128$	0.08	0.00072	140	3.6
cB211.072.96	1.778	$96^3 \times 192$	0.08	0.00072	140	5.4
cC211.060.80	1.836	$80^3 \times 160$	0.07	0.00060	137	3.8
cC211.060.112	1.836	$112^3 \times 224$	0.07	0.00060	137	5.3
cD211.054.96	1.900	$96^3 \times 192$	0.06	0.00054	141	3.9
cE211.044.112	1.960	$112^3 \times 224$	0.05	0.00044	136	3.8
cA211.53.24	1.726	$24^3 \times 48$	0.09	0.00530	360	4.0
cA211.40.24	1.726	$24^3 \times 48$	0.09	0.00400	315	3.5
cA211.30.32	1.726	$32^3 \times 64$	0.09	0.00300	272	4.0
cA211.12.48	1.726	$48^3 \times 96$	0.09	0.00120	174	3.8
cB211.25.48	1.778	$48^3 \times 96$	0.08	0.0025	260	5.0
cB211.14.64	1.778	$64^3 \times 112$	0.08	0.0014	194	5.0

finite-size effects. The cE211.044.112 ensemble corresponds to our finest lattice spacing $a \approx 0.05$ fm. We remind that the cB211.074.96 and the cC211.060.112 ensembles, which have a spatial lattice size $L \approx 7.6$ fm, are used to estimate FSEs by comparing to the cB211.074.64 and cC211.060.80 ensembles of smaller spatial size, respectively. Note that for the ensembles listed in the upper part of Table II, which are the only ones that are used for the calculation of $a_\mu^{\rm HVP}(s)$ and $a_\mu^{\rm HVP}(c)$, the pion mass is simulated very close to the reference value $M_\pi = 135$ MeV. For the evaluation of the quark connected contribution to $a_\mu^{\rm HVP}(s)$ $[a_\mu^{\rm HVP}(c)]$, the inversions of the Dirac operator are performed using up to $N_{\rm hits} = 112$ ($N_{\rm hits} = 24$) spin-diluted spatial stochastic sources per gauge configuration.

APPENDIX B: SCHEME DEFINING ISOSPIN SYMMETRIC $N_f = 2+1+1$ QCD

In this appendix, we describe in detail the procedure that we use to fine-tune the bare parameters of our lattice action, i.e. the determination of the parameters $m_{\rm cr}$, $m_\ell^{\rm iso}$, $m_s^{\rm iso}$ and $m_c^{\rm iso}$.

Our target definition of isoQCD is the one corresponding to the Edinburgh/FLAG consensus [27,28] and is implemented by using the hadronic inputs given in Eq. (12) to determine, at any fixed value of the strong bare coupling g_0, the bare quark masses $m_f^{\rm iso}$ and the lattice spacing $a^{\rm iso}$.

In Appendix A (see also Ref. [23] for more details) we discussed the strategy used to set the bare parameters $\mu_i^{\rm sim}$ of the Monte Carlo simulations and, therefore, also the corresponding matched parameters $m_f^{\rm sim}$ [see Eq. (A11) and text below it]. Since the conditions that we used to fix $m_f^{\rm sim}$ correspond to an alternative possible definition of isoQCD, that in fact differs from the Edinburgh/FLAG one for corrections that are of the order of isospin breaking effects on hadronic quantities, it turns out that the differences $m_f^{\rm iso} - m_f^{\rm sim}$ are very small. Moreover, the tuning of the chiral symmetry breaking bare parameter $m_{\rm cr}^{\rm sim}$ achieved at the time in which the Monte Carlo simulations have been performed is very accurate and, consequently, also the difference $m_{\rm cr} - m_{\rm cr}^{\rm sim}$ is very small, of the order of the statistical errors on $m_{\rm PCAC}$ [see Eq. (A14)]. By relying on these observations, we split the reweighting factors $W_f(m_f, m_{\rm cr})$ defined in Eq. (A13) according to

$$\begin{aligned} W_f(m_f, m_{\rm cr}) &= \hat{W}_f(m_{\rm cr})\bar{W}_f(m_f), \\ \hat{W}_f(m_{\rm cr}) &= \frac{\mathcal{D}^f_{\rm OS}(m_f^{\rm sim}, m_{\rm cr})}{\mathcal{D}^f_{\rm OS}(m_f^{\rm sim}, m_{\rm cr}^{\rm sim})}, \\ \bar{W}_f(m_f) &= \frac{\mathcal{D}^f_{\rm OS}(m_f, m_{\rm cr})}{\mathcal{D}^f_{\rm OS}(m_f^{\rm sim}, m_{\rm cr})}, \end{aligned} \tag{B1}$$

and expanded them in powers of the differences

$$\Delta m_f = m_f - m_f^{\rm sim}, \qquad \Delta m_{\rm cr} = m_{\rm cr} - m_{\rm cr}^{\rm sim}, \tag{B2}$$

which are treated as being of equal order, $O(\Delta m)$, and we neglect $O(\Delta m^2)$ corrections. Therefore, the formulas used to evaluate the reweighting factors are

$$\begin{aligned}\hat{W}_f(m_{\rm cr}) &= 1 + \Delta m_{\rm cr}{\rm Tr}\left[(-ir_f\gamma_5)\frac{1}{D^{\rm sim}_{\rm OS}}\right] \\ &\quad + O(\Delta m)^2, \\ \bar{W}_f(m_f) &= 1 + \Delta m_f {\rm Tr}\left[\frac{1}{D^{\rm sim}_{\rm OS}}\right] + O(\Delta m)^2, \end{aligned} \tag{B3}$$

where we use the compact operator notation

$$D^{\rm sim}_{\rm OS} = \gamma_\mu \overline{\nabla}_\mu[U] - ir_f\gamma_5(W^{\rm cl}[U] + m^{\rm sim}_{\rm cr}) + m^{\rm sim}_f. \tag{B4}$$

These formulas have been employed to evaluate the sea quark contribution to the derivatives of physical observables with respect to the critical mass and the bare quark masses, as we are now going to explain.

Any physical quantity O is calculated by taking its path-integral expectation value according to

$$O = \frac{\langle O[U]\prod_f \hat{W}_f(m_{\rm cr})\bar{W}_f(m_f)\rangle^{\rm sim}}{\langle \prod_f \hat{W}_f(m_{\rm cr})\bar{W}_f(m_f)\rangle^{\rm sim}}, \tag{B5}$$

where $O[U]$ denotes the Wick contractions at fixed gauge configuration U relevant for O and the expectation value $\langle\cdot\rangle^{\rm sim}$ includes the simulated probabilistic weight $P^{\rm sim}[U]$ given in Eq. (A10). By using Eq. (B3) and by expanding the previous formula at first order with respect to the mass differences we have

$$O = O^{\rm sim} + \Delta m_{\rm cr}\partial^{\rm sea}_{cr} O + \sum_f \Delta m_f \partial^{\rm sea}_f O, \tag{B6}$$

where $O^{\rm sim} = \langle O[U]\rangle^{\rm sim}$, the derivative with respect to the sea critical mass is given by

$$\begin{aligned}\partial^{\rm sea}_{cr} O &= \left\langle O[U]\sum\nolimits_f {\rm Tr}\left[(-ir_f\gamma_5)\frac{1}{D^{\rm sim}_{\rm OS}}\right]\right\rangle^{\rm sim} \\ &\quad - \langle O[U]\rangle^{\rm sim}\sum_f \left\langle {\rm Tr}\left[(-ir_f\gamma_5)\frac{1}{D^{\rm sim}_{\rm OS}}\right]\right\rangle^{\rm sim}, \end{aligned} \tag{B7}$$

and the derivative with respect to the sea mass of the f-flavour is given by

$$\partial^{\rm sea}_f O = \left\langle O[U]\,{\rm Tr}\left[\frac{1}{D^{\rm sim}_{\rm OS}}\right]\right\rangle^{\rm sim} - \langle O[U]\rangle^{\rm sim}\left\langle {\rm Tr}\left[\frac{1}{D^{\rm sim}_{\rm OS}}\right]\right\rangle^{\rm sim}. \tag{B8}$$

We use Eqs. (B6)–(B8) to calculate the sea-quark contribution to the variation of a physical quantity O under a small change Δm_f (or $\Delta m_{\rm cr}$) in the quark mass m_f (or the critical mass $m_{\rm cr}$). So far, our discussion is focused on the variation of O as the sea-quark masses and critical mass vary, with the valence quark masses entering O held constant.

To explain the procedure we implemented for determining $m^{\rm iso}_f$ (for $f = \ell, s, c$) and $m_{\rm cr}$, it is helpful to treat separately the dependencies of the observable $\mathcal{O}$ on the flavour quark masses (m_f) and the critical mass parameter $m_{\rm cr}$ that after use of the Wick theorem arise from the fermionic determinant (sea quark effects) and from the relevant quark propagators (valence quark effects). In fact, in the intermediate steps of our procedure for tuning $m^{\rm iso}_f$ and $m_{\rm cr}$ (see below), a given mass parameter, for practical reasons, can temporarily assume different values in the quark determinants (sea quark mass parameters) and in the quark propagators (valence quark mass parameters, which we label with a superscript "val"). For this reason, we rewrite Eq. (B6) in the following notation:

$$\begin{aligned}O(m_f, m_{\rm cr}|m^{\rm val}_f, m^{\rm val}_{\rm cr}) &\equiv \mathcal{O}^{\rm sim}(m^{\rm val}_f, m^{\rm val}_{\rm cr}) \\ &\quad + (m_{\rm cr} - m^{\rm sim}_{\rm cr})\partial^{\rm sea}_{\rm cr} O \\ &\quad + \sum_f (m_f - m^{\rm sim}_f)\partial^{\rm sea}_f O, \end{aligned} \tag{B9}$$

where on the lhs $O \equiv O(m_f, m_{\rm cr}|m^{\rm val}_f, m^{\rm val}_{\rm cr})$ and the first set of variables in the argument denotes the sea quark mass parameters while the second set refers to the valence quark mass parameters. On the rhs of Eq. (B9) $O^{\rm sim} \equiv O(m^{\rm sim}_f, m^{\rm sim}_{\rm cr}|m^{\rm val}_f, m^{\rm val}_{\rm cr}) \equiv \mathcal{O}^{\rm sim}(m^{\rm val}_f, m^{\rm val}_{\rm cr})$ denotes O computed with valence quark mass parameters $m^{\rm val}_f$ and $m^{\rm val}_{\rm cr}$ at sea quark mass parameters $m^{\rm sim}_f$ and $m^{\rm sim}_{\rm cr}$.

We are now in position to discuss the procedure that in practice we follow to match the Edinburgh/FLAG definition of isosymmetric QCD. In order to evaluate the dependence of $\mathcal{O}^{\rm sim}(m^{\rm val}_f, m^{\rm val}_{\rm cr})$ on the *valence* quark masses $m^{\rm val}_f$, in general we perform the inversion of the Dirac operator using a few values of $m^{\rm val}_f$ for all quark flavors, while keeping the valence critical mass parameter fixed at $m^{\rm val}_{\rm cr} = m^{\rm sim}_{\rm cr}$. Instead, in order to study the $m^{\rm val}_{\rm cr}$-dependence of $\mathcal{O}^{\rm sim}(m^{\rm val}_f, m^{\rm val}_{\rm cr})$, we explicitly evaluate the derivative

$$\partial^{\rm val}_{\rm cr} O \equiv \partial_{m^{\rm val}_{\rm cr}} \mathcal{O}^{\rm sim}(m^{\rm val}_f, m^{\rm val}_{\rm cr}). \tag{B10}$$

At this stage we can conveniently set $m^{\rm val}_{\rm cr} = m_{\rm cr}$, which allows us to write

$$\begin{aligned}O(m_f, m_{\rm cr}|m^{\rm val}_f, m_{\rm cr}) &= \mathcal{O}^{\rm sim}(m^{\rm val}_f, m^{\rm sim}_{\rm cr}) \\ &\quad + (m_{\rm cr} - m^{\rm sim}_{\rm cr})[\partial^{\rm sea}_{\rm cr} O + \partial^{\rm val}_{\rm cr} O] \\ &\quad + \sum_f (m_f - m^{\rm sim}_f)\partial^{\rm sea}_f O. \end{aligned} \tag{B11}$$

The fine-tuning of $m_{\rm cr}$, i.e. the determination of the small mismatch $m_{\rm cr} - m_{\rm cr}^{\rm sim}$, can be carried out independently of the tuning of the quark masses $m_f \to m_f^{\rm iso}$. Indeed, on one hand $m_{\rm cr} = a^{-1} w_{\rm cr}(g_0^2, a m_f)$, as determined by the condition of vanishing $m_{\rm PCAC}$ in twisted-mass lattice QCD, depends very weakly (actually only at $\mathrm{O}(a)$ level for $m_{\rm cr}$) on the values of the individual quark masses m_f. On the other hand the values of $m_f^{\rm sim}$ at which $m_{\rm PCAC}$ [see Eq. (A14)] is evaluated are quite close to the target values $m_f^{\rm iso}$ and the value of $m_{\rm cr}^{\rm sim}$ determined in the early stages of the Monte Carlo simulation differ from zero by a small amount, which is always (in modulus) below $0.06 m_\ell^{\rm sim}$ and typically different from zero by two to six standard deviations [75]. For these reasons, within the linear approximation approach we follow here, the differences Δm_f, $f = \ell, s, c$ [see Eq. (B2)] can safely be treated as negligible second order effects in the determination of $\Delta m_{\rm cr} = m_{\rm cr} - m_{\rm cr}^{\rm sim}$.

Thus, considering $O = m_{\rm PCAC}$ [see Eq. (A14)] expressed in the notation of Eq. (B9) and making use of Eq. (B11), we determine $m_{\rm cr}$ by solving the equation

$$\begin{aligned} &m_{\rm PCAC}(m_f^{\rm sim}; m_{\rm cr}|m_f^{\rm sim}, m_{\rm cr}) \\ &= m_{\rm PCAC}(m_f^{\rm sim}, m_{\rm cr}^{\rm sim}|m_f^{\rm sim}, m_{\rm cr}^{\rm sim}) \\ &\quad + (m_{\rm cr} - m_{\rm cr}^{\rm sim})[\partial_{\rm cr}^{\rm sea} + \partial_{\rm cr}^{\rm val}] m_{\rm PCAC} = 0. \end{aligned} \tag{B12}$$

In Fig. 9, we present the derivatives of $m_{\rm PCAC}$ with respect to the valence quark ($\partial_{\rm cr}^{\rm val} m_{\rm PCAC}$) and sea quark ($\partial_{\rm cr}^{\rm sea} m_{\rm PCAC}$) critical mass for the cB211.072.64 ensemble. As illustrated, both valence- and sea-quark contributions are of the same sign. However, the magnitude of the valence-quark contribution is approximately an order of magnitude smaller than that of the sea-quark contribution. The cB211.072.64 ensemble is the only one for which we have computed the valence-quark mass derivative $\partial_{\rm cr}^{\rm val} m_{\rm PCAC}$. For the C-type and D-type ensembles, we focused on the dominant sea-quark derivative alone, introducing an additional 10% uncertainty to account for the uncomputed valence-quark term. For the cE211.044.112 ensemble, where neither the valence- nor sea-quark contributions to the derivative are available, we estimated $[\partial_{\rm cr}^{\rm val} + \partial_{\rm cr}^{\rm sea}] m_{\rm PCAC}$ by using the D-type ensemble derivative as a central value. We then included a systematic uncertainty based on the observed difference between the C-type and D-type ensemble derivatives.

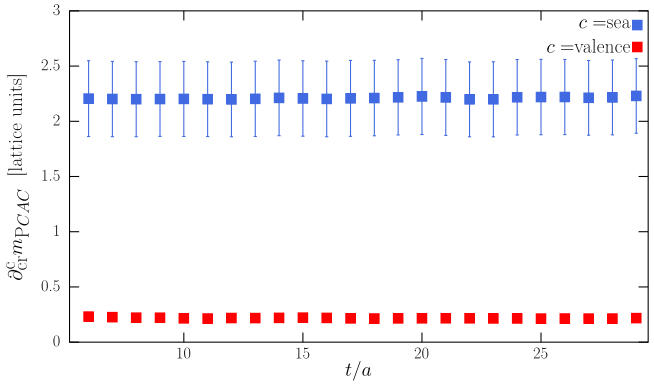

FIG. 9. Sea-quark (blue) and valence-quark (red) contribution to the derivative of the $m_{\rm PCAC}$ mass defined in Eq. (A14), as a function of the Euclidean time t/a on the cB211.072.64 ensemble.

Having fine-tuned the critical mass by determining the small difference $m_{\rm cr} - m_{\rm cr}^{\rm sim}$ for all lattice spacings employed in the present analysis, we now proceed to discuss the conditions that determine the quark masses $m_f^{\rm iso}$ as needed to match our definition of isosymmetric QCD given in Eq. (12). To simplify the notation, we set from now on

$$O(m_f|m_f^{\rm val}) \equiv O(m_f, m_{\rm cr}|m_f^{\rm val}, m_{\rm cr}). \tag{B13}$$

From the theoretical perspective, the solution $m_{f=\ell,s,c}^{\rm iso}$ of our tuning problem is obtained by solving the following system of equations

$$\begin{aligned} O^i(m_f^{\rm iso}|m_f^{\rm iso}) &= O^i(m_f^{\rm sim}|m_f^{\rm iso}) \\ &\quad + \sum_f [m_f^{\rm iso} - m_f^{\rm sim}] \partial_f^{\rm sea} O^i(m_f^{\rm sim}|m_f^{\rm iso}) \\ &= [O^i]^{\rm iso}, \end{aligned} \tag{B14}$$

where

$$O^i = \left\{ \frac{aM_\pi}{aF_\pi}, \frac{aM_K}{aF_\pi}, \frac{aM_{D_s}}{aF_\pi} \right\}, \tag{B15}$$

and then by defining the lattice spacing according to

$$a^{\rm iso} = \frac{aF_\pi(m_f^{\rm iso}|m_f^{\rm iso})}{F_\pi^{\rm iso}}. \tag{B16}$$

In practice, we solve the system by implementing an iterative procedure that we are now going to explain in detail. An illustrative sketch of this procedure is also shown in Fig. (10).

Before starting the iteration we have the following

$$\begin{aligned} &\texttt{Initialization Step: } i = 0, \\ &m_f^{(i)} = m_f^{\rm sim}, \quad a^{(i)} \equiv \frac{aF_\pi(m_{\ell,s,c}^{(i)}|m_\ell^{(i)})}{F_\pi^{\rm iso}}, \end{aligned} \tag{B17}$$

where i is the iteration index, and we are using the fact that aF_π does not depend on the strange and charm valence masses. The iteration then starts and runs on the flavor index that we order from lighter to heavier, namely

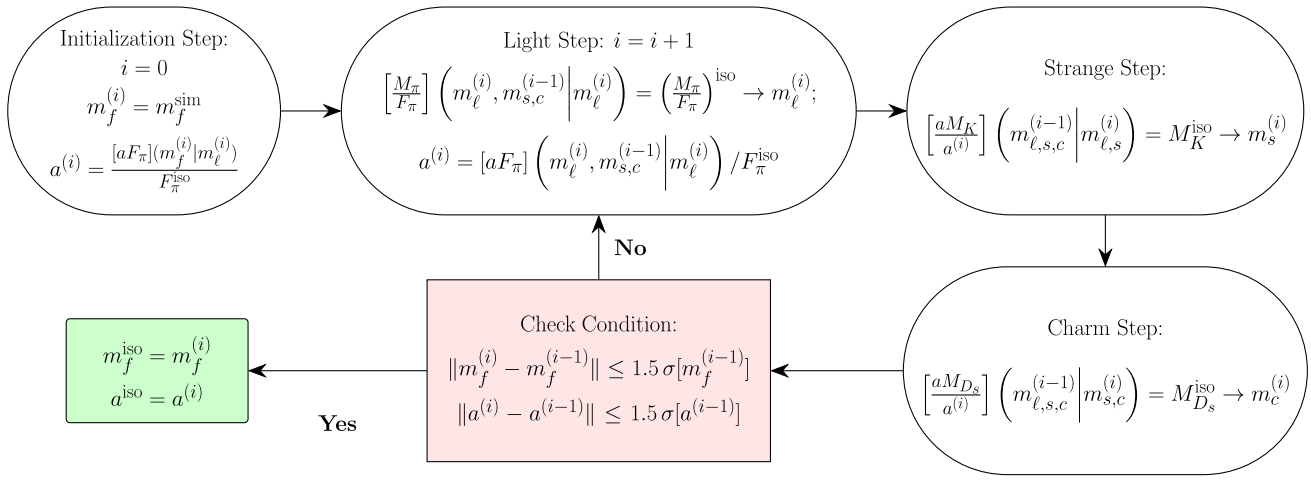

FIG. 10. Schematic description of the iterative algorithm used to determine $m_f^{\rm iso}$, which is described in detail in the text below. At each iteration, we update the values of the quark masses and of the lattice spacing until convergence is achieved. In the convergence condition, shown in the pink box, $\sigma[X]$ denotes the full (mostly statistical) error on X, for $X = m_f^{(i-1)}, a^{(i-1)}$.

$f = \ell, s, c$. To improve the tuning of the light quark mass and of the lattice spacing we implement the following

$$\begin{aligned}&\texttt{Light Step: } i = i+1,\\ &\left[\frac{aM_\pi}{aF_\pi}\right](m_\ell^{(i)}, m_{s,c}^{(i-1)}|m_\ell^{(i)}) = \left[\frac{M_\pi}{F_\pi}\right]^{\rm iso} \longrightarrow m_\ell^{(i)},\\ &a^{(i)} \equiv \frac{aF_\pi(m_\ell^{(i)}, m_{s,c}^{(i-1)}|m_\ell^{(i)})}{F_\pi^{\rm iso}},\end{aligned} \tag{B18}$$

where again we are using the fact that aM_π and aF_π do not depend upon the strange and charm valence masses.

In all steps, as already mentioned in the text above, the valence quark masses are changed by performing the needed valence-quark propagator inversions required to compute the input observables.

To improve the tuning of the strange quark mass we then implement the following

$$\texttt{Strange Step: } \left[\frac{aM_K}{a^{(i)}}\right](m_{\ell,s,c}^{(i-1)}|m_{\ell,s}^{(i)}) = M_K^{\rm iso} \longrightarrow m_s^{(i)}. \tag{B19}$$

Here we are using the fact that aM_K does not depend upon the charm valence masses.

To improve the tuning of the charm quark mass we then implement the following

$$\texttt{Charm Step: } \left[\frac{aM_{D_s}}{a^{(i)}}\right](m_{\ell,s,c}^{(i-1)}, |m_{s,c}^{(i)}) = M_{D_s}^{\rm iso} \longrightarrow m_c^{(i)}. \tag{B20}$$

At the end of the Charm-Step the lattice spacing and all quark masses are updated, and we check whether we reach the target precision given by the following convergence condition

$$\begin{aligned}&\texttt{Check Condition:}\\ &\texttt{if } \|m_f^{(i)} - m_f^{(i-1)}\| \le \frac{3}{2}\sigma[m_f^{(i-1)}]\\ &\texttt{and } \|a^{(i)} - a^{(i-1)}\| \le \frac{3}{2}\sigma[a^{(i-1)}]\\ &\quad m_f^{\rm iso} = m_f^{(i)}, \quad a^{\rm iso} = a^{(i)},\\ &\quad \texttt{end}\\ &\texttt{else goto light-step}\end{aligned} \tag{B21}$$

where $\sigma[m_f^{(i-1)}]$ and $\sigma[a^{(i-1)}]$ are the statistical errors on the tuned quark masses and on the lattice spacing.

It turns out that at the end of the first iteration, $i = 1$, the convergence condition is not satisfied. The values of the simulated sea-quark masses $m_f^{\rm sim} = m_f^{(0)}$ differ from the quark masses $m_f^{(1)}$ by a few percent. The difference is between 2%–7% for $m_\ell^{(1)} - m_\ell^{(0)}$, and between 2%–4% for $m_s^{(1)} - m_s^{(0)}$ and $m_c^{(1)} - m_c^{(0)}$. We therefore continue to $i = 2$, incorporating the sea-quark mass corrections through the linear-reweighting approximation of Eq. (B9). The sea-quark mass corrections to aM_π, aF_π, aM_K and aM_{D_s} turn out to be extremely tiny. Compared to the statistical errors of the uncorrected quantities, they amount to at most 1.5σ for aF_π, about 1σ for aM_π and are completely negligible for aM_K and aM_{D_s}. This allows us to verify the condition in Eq. (B21) and to exit the loop at the end of the iteration $i = 2$.

We now give a separate description of the tuning steps described above and present our final results for the quark masses $m_f^{\rm iso}$.

(i) `Light Step`: To determine $m_\ell^{(i)}$ and $a^{(i)}$ at each step i, we employ two methods: the *direct* and *global fit* approaches. In the *direct* approach, starting from the values of aF_π and aM_π on the nearly physical ensembles of Table II, we apply Eq. (B9) to vary the light sea-quark mass, while in order to be able to perform the corresponding change in the valence sector we have produced data for aF_π and aM_π at a second value of $m_\ell^{\rm val} < m_\ell^{\rm sim}$. Since the nearly physical ensembles of Table II have pion masses which differ from $M_\pi^{\rm iso}$ at most by 5 MeV, the valence- and sea-quark mass corrections needed to match the Edinburgh/FLAG conditions are small, making the linear reweighting approximation reliable. To confirm this, we carry out a second type of analysis, based on a global fit of aF_π and M_π/F_π, exploiting all the ensemble in Table II, included those with larger-than-physical pion mass. The *global-fit* analysis has been already discussed in Appendix A (Sec. II) of Ref. [22], to which we refer for additional details. In a nutshell, for this analysis we perform a global fit of aF_π and am_ℓ, using all the ensembles of Table II, according to the following ChPT-inspired ansatz

$$\begin{aligned} aF_\pi(\xi_\pi,\beta) &= a\bar{F}_\pi(\beta)\cdot\{1-2\xi_\pi\log(\xi_\pi/\xi_\pi^{\rm iso}) \\ &\quad +[P+P_{\rm disc}(aF_\pi(\xi_\pi,\beta))^2](\xi_\pi-\xi_\pi^{\rm iso})\} \\ am_\ell(\xi_\pi,\beta) &= a\bar{m}_\ell(\beta)\frac{\xi_\pi}{\xi_\pi^{\rm iso}}\cdot\{1+5\xi_\pi\log(\xi_\pi/\xi_\pi^{\rm iso}) \\ &\quad +(B+a^2B_{\rm disc})(\xi_\pi-\xi_\pi^{\rm iso})\}^{-1}, \end{aligned} \tag{B22}$$

where $\beta = 6/g_0^2$ is the inverse QCD gauge coupling and

$$\xi_\pi = \frac{M_\pi^2}{16\pi^2F_\pi^2}. \tag{B23}$$

In Eq. (B22), $a\bar{F}_\pi(\beta)$, $a\bar{m}_\ell(\beta)$, P, $P_{\rm disc}$, B and $B_{\rm disc}$ are free-fit parameters (for $a\bar{F}_\pi(\beta)$ and $a\bar{m}_{\ell(\beta)}$ there is a different fit parameter for each β). In the global fit method, at each iteration step, the (bare) light quark mass and the lattice spacing corresponding to the Edinburgh/FLAG definition of isosymmetric QCD are given, for each value of the coupling β, by

$$a^{(i)}(\beta) = \frac{a\bar{F}_\pi(\beta)}{F_\pi^{\rm iso}}, \qquad m_\ell^{(i)}(\beta) = \bar{m}_\ell(\beta). \tag{B24}$$

The hadronic observables F_π and M_π (and hence ξ_π) entering Eq. (B22) are intended as infinite-volume quantities. The needed infinite-volume extrapolation of our lattice data is carried out by employing next-to-leading-order ChPT, i.e. making use of the Gasser-Leutwyler formulae [76]. We have checked that next-to-leading-order ChPT nicely describes the spread between the F_π and M_π values on the ensembles of Table II produced at different values of the spatial volume, but equal values of β and quark masses.

The advantage of the global fit approach is that it captures the dependence of both F_π and M_π/F_π on m_ℓ without relying on leading-order reweighting, instead utilizing gauge ensembles generated away from the physical point (we emphasize that all data contributing to the global fit in Eq. (B22) were produced at different values of m_ℓ, but for each ensemble, the valence light-quark mass is equal to the sea light-quark mass).

In Fig. 11, we show the result of the global fit and compare it with that of the direct approach, which as already stressed, only uses the nearly physical ensembles of Table II, and relies on leading-order reweighting to describe the light sea-quark mass dependence of M_π and F_π. The reduced χ^2 of the global fit to aF_π and am_ℓ is very good, about 0.5. The results in the two figures correspond to the global fit performed during the first light-step iteration ($i = 1$), where the strange and charm sea-quark masses are held fixed to their simulation value $m_{s,c}^{\rm sim}$. As the figures show, the agreement between the two approaches is excellent; the difference between the two determinations of $m_\ell^{(1)}$ and $a^{(1)}$ is smaller than the statistical uncertainty.

Two remarks are relevant here. First, as it is shown by Eq. (B18), during the ith light-step the strange and charm quark masses are held fixed to the value obtained at the $(i-1)$th iteration, and therefore for $i = 1$ they are set to the simulated values $m_{s,c}^{(i=1)} = m_{s,c}^{\rm sim}$. At the end of the first iteration we do not reach convergence, and therefore in the second iteration ($i = 2$) we proceed by adding the strange and charm sea-quark corrections to F_π and M_π according to Eq. (B9). These corrections in practice have only the effect of increasing slightly the uncertainty on the determination of m_ℓ and of the lattice spacing. In the panels on the right of Fig. 11 we add, for comparison, the results obtained for $m_\ell^{(2)}$ and $a^{(2)}F_\pi^{\rm iso}$, which then also correspond to our final results for $m_\ell^{\rm iso}$ and $a^{\rm iso}$. Indeed, after the second iteration we achieve convergence, and hence exit the loop.

The second comment concerns the corrections to F_π and M_π that stem from the small-mistuning, $m_{\rm cr} - m_{\rm cr}^{\rm sim}$, of the critical mass. These corrections may of course be included by adding the second

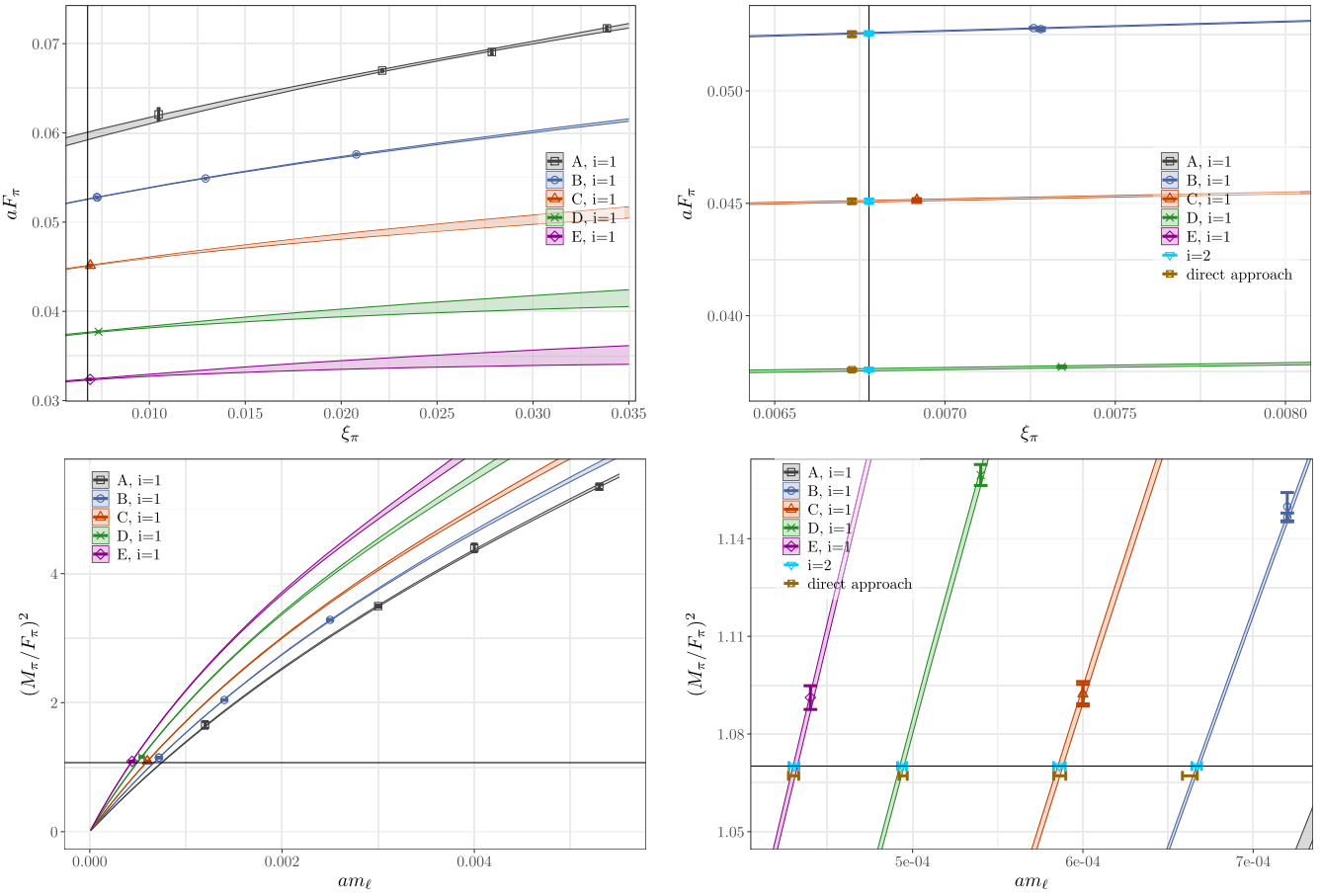

FIG. 11. Results of the global fit to aF_π (top panels) and am_ℓ (bottom panels). The colored bands correspond to the best fit curve obtained in the global fit at each value of β, while the data points to our determination of aF_π and $(M_\pi/F_\pi)^2$ on each of the gauge ensembles of Table II. The rightmost plots show a zoom in the region close to the physical point, where, for comparison, we include the result obtained using the direct approach at the iteration $i = 1$ (data points in brown), and the final result after the iteration $i = 2$ (data points in sky-blue), i.e. after inserting the charm and strange sea-quark mass corrections making use of Eq. (B9). In these plots, the vertical and horizontal lines correspond to the point $\xi_\pi = \xi_\pi^{\rm iso}$. In the bottom-right (top-right) plot the data points in brown, corresponding to the results of the direct approach at the iteration $i = 1$, are slightly shifted vertically (horizontally) for better visualization.

term in Eq. (B11). In the specific case of M_π and F_π, however, to include such corrections, one can also profit from the existence of the following analytic expression [25], for the leading, $\mathcal{O}(a^0)$, dependence of M_π and F_π on the $m_{\rm PCAC}$ mass

$$F_\pi(m_{\rm PCAC}=0) = F_\pi(m_{\rm PCAC}) \times \sqrt{1+(Z_A m_{\rm PCAC}/m_\ell)^2}$$
$$M_\pi^2(m_{\rm PCAC}=0) = \frac{M_\pi^2(m_{\rm PCAC})}{\sqrt{1+(Z_A m_{\rm PCAC}/m_\ell)^2}}, \qquad \text{(B25)}$$

where Z_A (see Appendix E) is the renormalization constant of the axial current. We have employed the analytic expressions (B25) to correct F_π and M_π on all the ensembles of Table II, included those with higher-than-physical pion masses, for which a first-principle estimate of the critical mass derivative in Eq. (B11) is not available to us. We have explicitly checked, in the case of the nearly physical ensembles of Table II, that the corrections produced by the analytic expressions above, agree within uncertainties with the numerical results from the second term in the rhs of Eq. (B11).

(ii) `Strange Step`: The determination of the strange-quark mass $m_s^{\rm iso}$ (as well as of the charm quark mass to be discussed in the next bullet point), turns out to be substantially less involved than the determination of $m_\ell^{\rm iso}$ and of the lattice spacing.

For this analysis, we have employed only the nearly physical ensemble of Table II, which as already remarked, are the only ones entering the analysis of $a_\mu^{\rm HVP}(s)$ and $a_\mu^{\rm HVP}(c)$. At each iteration,

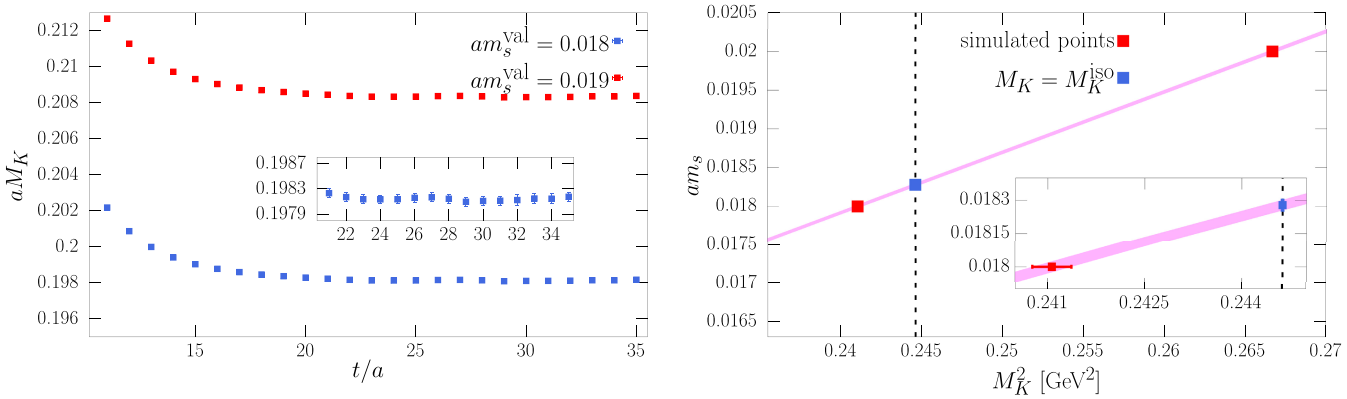

FIG. 12. Left: effective mass of the kaon for the two simulated values of the valence strange quark mass $am_s^{\rm val} = 0.018, 0.019$ on the cB211.072.64 ensemble. Right: interpolation of the strange quark mass am_s to the physical point defined by $M_K = M_K^{\rm iso} = 494.6$ MeV, indicated in the plot by the vertical dashed line. The interpolation has been performed according to the ansatz of Eq. (B26).

to be able to vary the valence light and strange quark masses we have performed the inversion of the two-point pseudoscalar light-strange correlator employing two values of $m_s^{\rm val}$ and two values of $m_\ell^{\rm val}$ (one of these two values is $m_\ell^{\rm val} = m_\ell^{\rm sim}$). The critical mass corrections due to the small difference $m_{\rm cr} - m_{\rm cr}^{\rm sim}$ have been included by adding the second term in the rhs of Eq. (B11) for $O = M_K$. This correction, however, turns out to be much smaller than the statistical errors and can safely be neglected. During the first iteration $i = 1$, the light, strange, and charm quark masses are fixed to their simulation value and therefore no correction has been applied. During the second iteration, $i = 2$, we have applied the corrections corresponding to the last term in Eq. (B11). Moreover, all the sea-quark mass corrections turn out to be extremely tiny and negligible. The only (small) difference between $m_s^{(1)}$ and $m_s^{(2)}$, comes from the slightly increased uncertainties on the lattice spacing. As already pointed out, at the end of the second iteration, we achieve convergence and exit the loop.

To illustrate the quality of the effective-mass plateaus, we show in the left panel of Fig. 12 the effective mass of the kaon, determined on the cB211b.072.64 ensemble, for the two different values of the valence strange quark mass employed for this calculation and for $m_\ell^{\rm val} = m_\ell^{\rm sim}$. The panel on the right shows instead the result of the final strange-mass interpolation needed to impose $M_K = M_K^{\rm iso}$, which we performed according to the following ChPT-inspired ansatz

$$m_s = A + BM_K^2, \tag{B26}$$

where A and B are fit parameters.

(iii) `Charm Step`: For charm mass tuning we have included in the analysis only the nearly physical ensembles of Table II. At each iteration, we vary the valence strange and charm quark masses and evaluate the two-point pseudoscalar strange-charm correlator employing up to two values of $m_s^{\rm val}$ and up to three values of $m_c^{\rm val}$. [6]

For aM_{D_s}, all the sea-quark mass and critical mass corrections, which have been included during the second iteration step $i = 2$ making use of Eq. (B11), turn out to be negligible within statistical uncertainty, and, as in the case of the strange-quark mass, the only difference between $m_c^{(1)}$ and $m_c^{(2)}$ comes from the slightly increased lattice spacing uncertainties.

To illustrate the quality of the effective-mass plateaus, we show in the left panel of Fig. 13 the effective mass of the D_s meson, determined on the cC211.060.112 ensemble, for the three different values of the charm quark mass and for the single value of the valence quark mass, $m_s^{\rm val} \sim m_s^{\rm iso}$, that we employed. The right panel plot shows instead the result of the final interpolation needed to impose $M_{D_s} = M_{D_s}^{\rm iso}$, which was performed according to the following ansatz

$$m_c = A + BM_{D_s}, \tag{B27}$$

where A and B are fit parameters. We have checked, on the ensembles where three different valence charm quark masses are employed, namely the cC211.060.112, the cD211.054.96, and the

[6]For the charm sea-quark mass corrections, the results obtained using leading-order reweighting turn out to be too noisy to be used. We estimate the charm sea-quark mass derivative $\partial_c^{\rm sea}$ from the strange sea-quark mass derivative $\partial_s^{\rm sea}$, assuming the scaling $m_c\partial_c^{\rm sea} \sim m_s\partial_s^{\rm sea}$ (see the discussion in Appendix D for more details on this point).

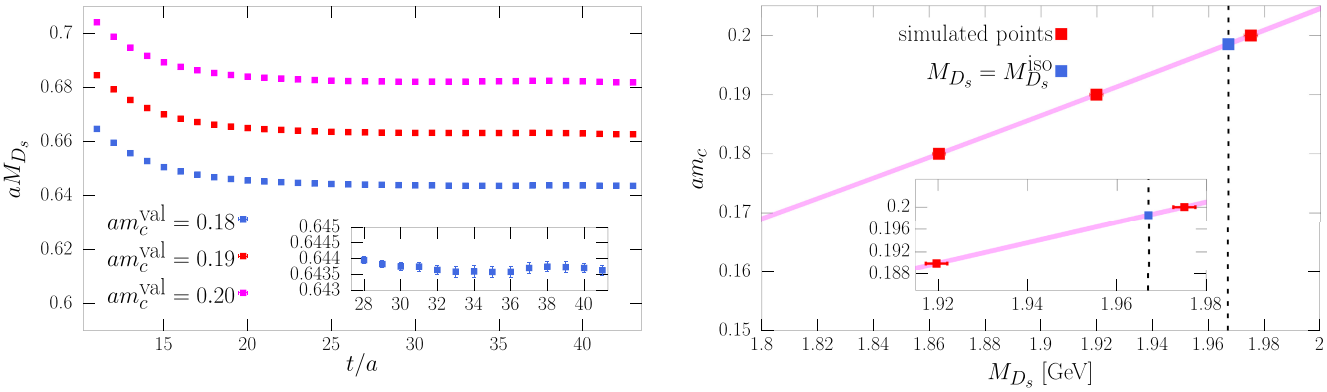

FIG. 13. Left: effective mass of the D_s meson for the three simulated values of the valence charm quark mass $am_c^{\rm val} = 0.18$, 0.19 and 0.20 on the cC211.060.112 ensemble. Right: interpolation of the charm quark mass am_c to the physical point defined by $M_{D_s} = M_{D_s}^{\rm iso} = 1967$ MeV, indicated in the plot by the vertical dashed line. The interpolation is performed according to the ansatz of Eq. (B27) including also a quadratic term proportional to $M_{D_s}^2$. However, the results at the physical point $M_{D_s} = M_{D_s}^{\rm iso}$, remain unchanged if a simple linear interpolation to the two rightmost red data points in the figure is performed.

cE211.044.112 ensemble, that the inclusion of a quadratic term proportional to $M_{D_s}^2$ in the interpolation, produces a negligible change in the value of $m_c^{(i)}$.

Having described all the tuning steps of the iterative procedure that allow us to match the Edinburgh/FLAG isosymmetric world, we collect in Table I the resulting values of the lattice spacing $a^{\rm iso}$, the critical mass $am_{\rm cr}$ and the quark masses $am_{\ell,s,c}^{\rm iso}$ for the four lattice spacings used in the calculation of $a_\mu^{\rm HVP}(s)$ and $a_\mu^{\rm HVP}(c)$. The values quoted in Table I for the lattice spacing have slightly larger uncertainties than the ones given in Ref. [77], due to the improved analysis of the sea-quark mistuning effects. However, the slightly increased uncertainty on the lattice spacing does not have any impact on the final values and errors quoted in Ref. [77].

We conclude this section with a brief description of the two lattice regulated versions of the electromagnetic current operator (called in Sec. III the TM and the OS currents) that we employ for the evaluation of $a_\mu^{\rm HVP}(s)$ and $a_\mu^{\rm HVP}(c)$. To define the TM bilinear operators, starting from the action in Eq. (A1), we introduce additional valence quark fields with no feedback on the gauge effective action. This amounts to (i) including, for each quark field q_f, $f = \{u, d, s, c\}$ appearing in Eq. (A4), a replica field q'_f with the same soft mass, $m'_f = m_f$, but opposite value of the Wilson parameter, $r'_f = -r_f$ and hence opposite critical mass, $m_{\rm cr}(r'_f) = -m_{\rm cr}(r_f)$; and (ii) adding the corresponding ghost field ϕ'_f, in order to remove any contributions of these extra fields to the fermionic determinants, i.e., to the lattice gauge effective action. In summary, to define the TM bilinears we add to the action S of Eq. (A1) the action term[7]

$$\begin{aligned} S^{\rm rep} = &\sum_f \sum_x \bar{q}'_f \{\gamma_\mu \overline{\nabla}_\mu[U] + i r_f \gamma_5 (W^{\rm cl}[U] + m_{\rm cr}) + m_f\} q'_f \\ &+ \sum_f \sum_x \bar{\phi}'_f \{\gamma_\mu \overline{\nabla}_\mu[U] + i r_f \gamma_5 (W^{\rm cl}[U] + m_{\rm cr}) \\ &+ m_f\} \phi'_f, \end{aligned} \tag{B28}$$

i.e., we work with the mixed lattice action $S^{\rm mixed} = S + S^{\rm rep}$. The TM quark bilinears are then defined as

$$J_\Gamma^{\rm TM}(x) = \bar{q}_f(x) \Gamma q'_f(x), \tag{B29}$$

with Γ a generic Dirac matrix, and in particular the TM electromagnetic current is given by

$$J_f^{\mu,{\rm TM}}(x) = Z_A q_{{\rm em},f} \bar{q}_f(x) \gamma^\mu q'_f(x), \quad f = \{s, c\}, \tag{B30}$$

where Z_A is the renormalization constant of the current that in the unitary regularization with untwisted Wilson quarks would be the axial current. To define the corresponding OS version of quark bilinear operators, we do not need in principle to introduce any additional replica

[7]On the cC211.060.112, cD211.054.96 and cE211.044.112 ensembles, we have considered a single value of $m_s^{\rm val}$, carefully chosen to be very close to $m_s^{(1)} \sim m_s^{(2)} = m_s^{\rm iso}$. We have checked, using our determination of the slope $\partial M_{D_s}/\partial m_s^{\rm val}$ on the ensembles where results at two different values of the valence strange-quark mass are available, that the small difference $m_s^{\rm val} - m_s^{(i)}$, produces a completely negligible impact on the determination of $m_c^{(i)}$.

valence fields, since the OS bilinears are constructed in terms of the quark fields q_f entering the OS quark action defined in Eq. (A4). However, in order to single out the connected part of a two-point correlation function of OS bilinears, we find it convenient to add to the action S of Eq. (A1) the valence quark action term of Eq. (B28) with the replacement $r'_f \to -r'_f = -r_f$. In terms of the quark fields q_f and of the replica valence fields q'_f, with $r'_f = r_f$, the OS electromagnetic current is thus given by

$$J^{\mu,\mathrm{OS}}_f(x) = Z_V q_{\mathrm{em},f} \bar{q}_f(x)\gamma^\mu q'_f(x), \quad f = \{s,c\}, \tag{B31}$$

where Z_V is the renormalization constant of the current that in the unitary regularization with untwisted Wilson quarks would (also) be the vector current (see Appendix E). In the lattice setup of interest here with action $S^{\mathrm{mixed}} = S + S^{\mathrm{rep}}$, the vector channel correlators V^{TM}_f and V^{OS}_f entering in the rhs of Eq. (13) are then defined as

$$\begin{aligned} V^{\mathrm{TM}}_f(t) &\equiv \frac{1}{3}\sum_{\mathbf{x}}\sum_{i=1,2,3}\langle J^{i,\mathrm{TM}}_f(x)[J^{i,\mathrm{TM}}_f]^\dagger(0)\rangle, \\ V^{\mathrm{OS}}_f(t) &\equiv \frac{1}{3}\sum_{\mathbf{x}}\sum_{i=1,2,3}\langle J^{i,\mathrm{OS}}_f(x)[J^{i,\mathrm{OS}}_f]^\dagger(0)\rangle, \end{aligned} \tag{B32}$$

Two-point correlation functions constructed in terms of the TM or OS bilinears, such as $V^{\mathrm{TM}}_f(t)$ and $V^{\mathrm{OS}}_f(t)$, produce equivalent results in the continuum limit [72]. At nonzero values of the lattice spacing a, they however differ by $\mathcal{O}(a^2)$ UV cutoff effects and, as explained in the main text, we exploit this fact to perform joint fits of the results obtained with the two regularizations while enforcing a common continuum-limit.

APPENDIX C: EVALUATING THE HVP AT THE ISOQCD POINT

To evaluate the strange and charm HVP, along with the corresponding SD, LD and W contributions, at the Edinburgh/FLAG isoQCD point, see Eq. (12), we exploited all gauge ensembles in the upper part of Table II. For each ensemble, we performed the inversions of the vector TM and OS correlators of Eq. (B32), for different valence quark masses m_s^{val} and m_c^{val}, while fixing sea-quark masses and critical mass to m_f^{sim} and $m_{\mathrm{cr}}^{\mathrm{sim}}$, respectively. For each β, we carefully chose two values for m_s^{val} and three values for m_c^{val}, in such a way that they are always rather close to m_s^{iso} and m_c^{iso}.

Adopting the notation of Eq. (B9), we first performed the required valence quark-mass interpolation of both $a_\mu^{\mathrm{HVP,w}}(s)(m_f^{\mathrm{sim}}, m_{\mathrm{cr}}^{\mathrm{sim}}|m_s^{\mathrm{val}}, m_{\mathrm{cr}}^{\mathrm{sim}})$ and $a_\mu^{\mathrm{HVP,w}}(c)(m_f^{\mathrm{sim}}, m_{\mathrm{cr}}^{\mathrm{sim}}|m_c^{\mathrm{val}}, m_{\mathrm{cr}}^{\mathrm{sim}})$, using the following ansatz

$$\begin{aligned} a_\mu^{\mathrm{HVP,w}}(c)(m_f^{\mathrm{sim}}, m_{\mathrm{cr}}^{\mathrm{sim}}|m_c^{\mathrm{val}}, m_{\mathrm{cr}}^{\mathrm{sim}}) &= a_\mu^{\mathrm{HVP,w}}(c)(m_f^{\mathrm{sim}}, m_{\mathrm{cr}}^{\mathrm{sim}}|m_c^{\mathrm{iso}}, m_{\mathrm{cr}}^{\mathrm{sim}})\cdot[1 + A_c^w(m_c^{\mathrm{val}} - m_c^{\mathrm{iso}}) + B_c^w(m_c^{\mathrm{val}} - m_c^{\mathrm{iso}})^2] \\ a_\mu^{\mathrm{HVP,w}}(s)(m_f^{\mathrm{sim}}, m_{\mathrm{cr}}^{\mathrm{sim}}|m_s^{\mathrm{val}}, m_{\mathrm{cr}}^{\mathrm{sim}}) &= a_\mu^{\mathrm{HVP,w}}(s)(m_f^{\mathrm{sim}}, m_{\mathrm{cr}}^{\mathrm{sim}}|m_s^{\mathrm{iso}}, m_{\mathrm{cr}}^{\mathrm{sim}})\cdot[1 + A_s^w(m_s^{\mathrm{val}} - m_s^{\mathrm{iso}})], \end{aligned} \tag{C1}$$

where A_s^w, A_c^w and B_c^w, as well as $a_\mu^{\mathrm{HVP,w}}(s)(m_f^{\mathrm{sim}}, m_{\mathrm{cr}}^{\mathrm{sim}}|m_s^{\mathrm{iso}}, m_{\mathrm{cr}}^{\mathrm{sim}})$ and $a_\mu^{\mathrm{HVP,w}}(c)(m_f^{\mathrm{sim}}, m_{\mathrm{cr}}^{\mathrm{sim}}|m_c^{\mathrm{iso}}, m_{\mathrm{cr}}^{\mathrm{sim}})$, are fit parameters.

After interpolating $m_s^{\mathrm{val}} \to m_s^{\mathrm{iso}}$, and $m_c^{\mathrm{val}} \to m_c^{\mathrm{iso}}$, we applied the corrections needed to incorporate the effects of the fine-tuning of the critical mass and of the sea-quark mass parameters. As discussed in Appendix B, leading-order reweighting has been used to evaluate the sea-quark corrections, ultimately allowing us to determine the HVP at our isosymmetric point of reference by using Eq. (B11) with $m_f = m_f^{\mathrm{val}} = m_f^{\mathrm{iso}}$ and

$$O = \{a_\mu^{\mathrm{HVP,w}}(s), a_\mu^{\mathrm{HVP,w}}(c)\}. \tag{C2}$$

Appendix D provides a detailed discussion of the evaluation of the sea-quark mass and critical mass derivatives appearing in the rhs of Eq. (B11).

APPENDIX D: ESTIMATING EFFECTS OF MISTUNINGS OF SIMULATION PARAMETERS

In this section, we give some details on the calculation of the sea-quark mass corrections to the physical observables O relevant for the present analysis, which we performed by employing the leading-order reweighting discussed in Appendix B, i.e. making use of the formula in Eq. (B6).

The observables O, of which we discuss the sea-quark mass corrections in this appendix, are

$$O = \{M_\pi, F_\pi, M_K, M_{D_s}, a_\mu^{\mathrm{HVP}}(s), a_\mu^{\mathrm{HVP}}(c)\}. \tag{D1}$$

We start from the observables used to determine the quark masses m_f^{iso} and to set the scale, namely M_π, F_π, M_K and M_{D_s}. In Fig. 14 we show the results for the light and strange sea-quark mass derivatives of the effective pion mass and decay constant, $\partial^{\mathrm{sea}}_{\ell,s} M_\pi^{\mathrm{eff}}(t)$ and $\partial^{\mathrm{sea}}_{\ell,s} F_\pi^{\mathrm{eff}}(t)$, as obtained on the cB211.072.64 ensemble. As the figure shows, the absolute value of these quark-mass derivatives, as expected,

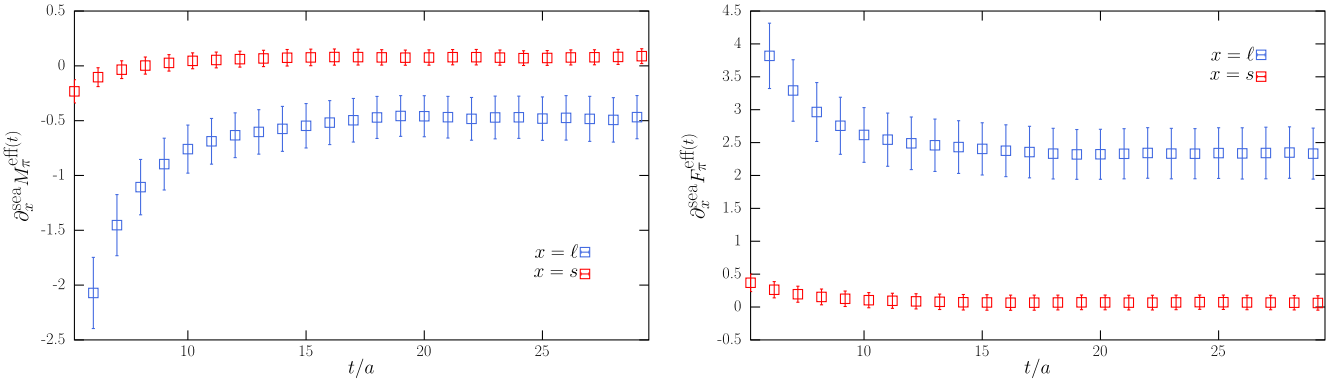

FIG. 14. The light and strange sea-quark mass derivatives of the effective pion mass (left) and of the effective pion decay constant (right), as a function of the Euclidean time on the cB211.072.64 ensemble.

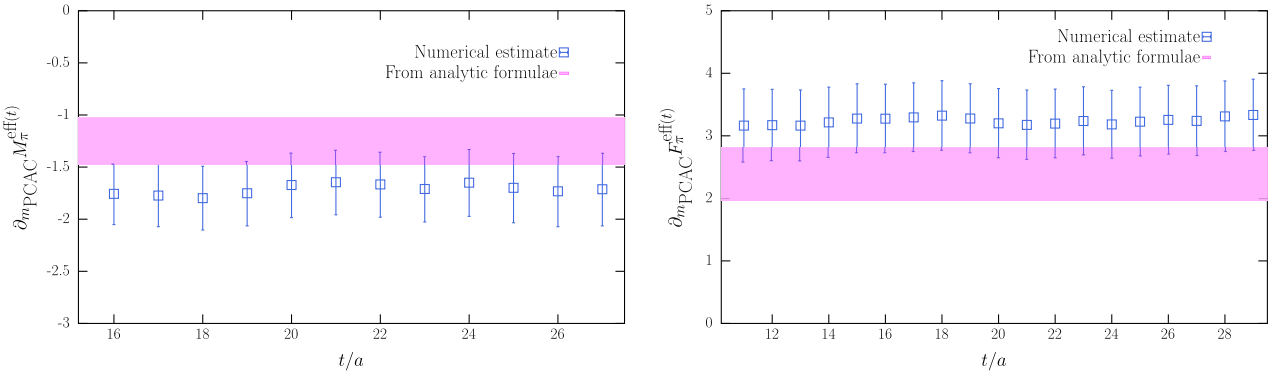

FIG. 15. The $m_{\rm PCAC}$-derivative of the effective pion mass (left) and of the effective pion decay constant (right) on the cC211.060.80 ensemble. The magenta bands correspond to the predictions of the analytic formulas of Eq. (B25).

strongly decreases as the quark mass increases (i.e. going from light to strange). The light-quark derivative is in absolute value larger for F_π than for M_π, by a factor of about 5. The largest mistuning in the bare ligth quark mass, $\Delta\bar{m}_\ell = m_\ell^{\rm iso} - m_\ell^{\rm sim}$, occurs on the cB211.072.64 and cD211.054.96 ensembles, for which $\Delta\bar{m}_\ell \simeq -0.16$ MeV, which then yields a correction to F_π of about 0.3–0.4 MeV, and to M_π smaller than 0.1 MeV.

For the strange-quark mass derivative the signal-to-noise is sensibly smaller than for the light-quark one. The typical size of these derivatives is $|\partial_s^{\rm sea} M_\pi| \sim 0.08$ and $|\partial_s^{\rm sea} F_\pi| \sim 0.12$. The largest mistuning in the bare strange quark mass, $\Delta\bar{m}_s = m_s^{\rm iso} - m_s^{\rm sim}$, occurs on the cC211.060.80 ensemble where $\Delta\bar{m}_s \sim -1.7$ MeV, which produces on this ensemble a correction to M_π of about 0.13 MeV and of about 0.2 MeV to F_π, i.e. at the level of 0.1% and 0.15%, respectively. For the charm quark, as already mentioned in footnote 6,[8] the sea-quark derivatives turn out to be too noisy to provide a useful determination of the corresponding mistuning correction. For all observables O, we include in the analysis an estimate of the derivative $\partial_c^{\rm sea} O$ which assumes the following approximate scaling of the sea quark mass derivative with the quark mass

$$\partial_c^{\rm sea} O \simeq \frac{m_s}{m_c} \partial_s^{\rm sea} O. \tag{D2}$$

The $1/m_c$ suppression of the derivative with respect to the sea quark mass of a generic observable O is expected in the (approximatively well realized) limit $m_c \gg m_s \sim \Lambda_{\rm QCD}$ on each gauge background at finite lattice spacing from its analytic expression Eq. (B8). Actually an even stronger suppression, as $1/m_c^2$, is predicted in the same limit up to lattice artifacts by perturbation theory. We thus regard the estimate in Eq. (D2) as a conservative one.

Concerning the critical mass corrections to F_π and M_π, as detailed in Appendix B, we rely on the analytic formulae of Eq. (B25). In Fig. 15, we however compare on the cC211.060.80 ensemble, for which the absolute value of the difference $\Delta m_{\rm cr} = m_{\rm cr} - m_{\rm cr}^{\rm sim}$ is maximal, the results obtained using Eq. (B25) with that obtained by evaluating numerically the second term in Eq. (B11) with

[8]Note the different sign, as compared to Eq. (A4), in front of the critical Wilson term with coefficient $i\gamma_5$, which is due to $r'_f = -r_f$.

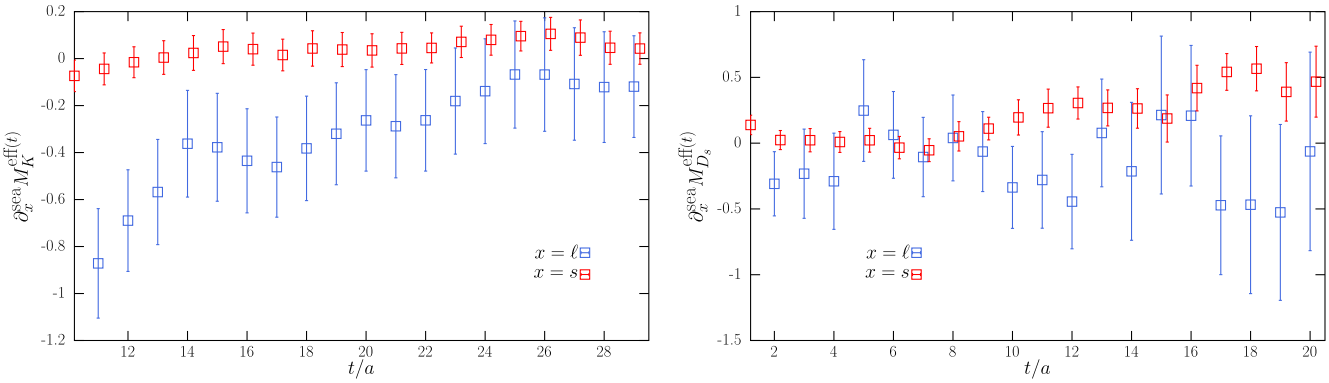

FIG. 16. The light and strange sea-quark mass derivatives of the effective kaon mass (left) and of the effective D_s-meson mass (right), as a function of the Euclidean time on the cB211.072.64 ensemble.

$O = M_\pi, F_\pi$. Specifically, in the figure we show the results for

$$\partial_{m_{\rm PCAC}} O \equiv \frac{\partial_{\rm cr} O}{\partial_{\rm cr} m_{\rm PCAC}}, \qquad O = \{M_\pi, F_\pi\}, \tag{D3}$$

where $\partial_{\rm cr} \equiv \partial_{\rm cr}^{\rm sea} + \partial_{\rm cr}^{\rm val}$ [see Eq. (B11)].[9] As the figure shows, the result of the numerical estimates and that of the analytic formulae of Eq. (B25) are in fairly good agreement.

We now move to the case of M_K and M_{D_s}. In Fig. 16 we show the results for the light and strange sea-quark mass derivatives of the effective mass of the kaon and of the D_s meson, as obtained on the cB211.072.64 ensemble. All derivatives turn out to be very small and compatible with zero within a few standard deviations. For the kaon mass M_K, the typical magnitude of the derivatives are: $|\partial_\ell M_K| \sim 0.2$, $|\partial_s M_K| \sim 0.1$. For the D_s-meson they are: $|\partial_\ell M_{D_s}| \sim 0.5$, $|\partial_s M_{D_s}| \sim 0.3$. The largest mistunings that we have are $\Delta m_\ell \simeq 0.16$ MeV, $\Delta m_s \simeq -1.7$ MeV. The largest correction to the kaon mass [including those from the fine-tuning of the critical mass, and from charm sea-quark mass mistuning estimated employing Eq. (D2)] is of about 0.2 MeV, while it is of about 0.5 MeV for M_{D_s}. In both cases, the corrections are smaller than our statistical uncertainties, hence completely negligible.

Finally, we discuss the mistuning corrections on $a_\mu^{\rm HVP}(s)$ and $a_\mu^{\rm HVP}(c)$. In this case, there are two different types of corrections. The first type of correction is an indirect one, arising from changes in the integration kernel function due to variations in the lattice spacing, which affects the definition of the physical time t in the integrand of Eq. (2). These corrections can be incorporated directly by evaluating the HVP using the lattice spacing values $a^{\rm iso}$ provided in Table I. The second source of corrections, which we now address, stems from the sea-quark mass and critical mass corrections to the vector correlators $V_s^{\rm reg}(t)$ and $V_c^{\rm reg}(t)$ in Eq. (B32). We introduce the following derivatives of $a_\mu^{\rm HVP}(s)$ and $a_\mu^{\rm HVP}(c)$ with respect to the sea-quark mass for the x-flavor and the (combined sea and valence) critical quark mass, while keeping the lattice spacing fixed at $a = a^{\rm iso}$:

$$\begin{aligned}
\partial_x^{\rm sea} a_\mu^{\rm HVP}(f) &= 2\alpha_{\rm em}^2 a^3 \sum_{n=1}^{T/(2a)} w(n) n^2 K(a m_\mu n) \partial_x^{\rm sea} V_f^{\rm reg}(na), \\
& \qquad f = s, c, \qquad x = \ell, s, c, \\
\partial_{\rm cr} a_\mu^{\rm HVP}(f) &= 2\alpha_{\rm em}^2 a^3 \sum_{n=1}^{T/(2a)} w(n) n^2 K(a m_\mu n) \\
& \qquad \times [\partial_{\rm cr}^{\rm sea} + \partial_{\rm cr}^{\rm val}] V_f^{\rm reg}(na), \qquad f = s, c.
\end{aligned} \tag{D4}$$

where $n = t/a = 1, \ldots, T/(2a)$ is the Euclidean time in lattice units. The derivatives of the SD, W and LD contributions can be defined analogously.

In Fig. 17, we present the results for the light and strange sea-quark mass derivatives of $a_\mu^{\rm HVP}(s)$ and $a_\mu^{\rm HVP}(c)$ as obtained on the cB211.072.64 and cD211.054.96 ensembles. The results correspond to reg = TM, but within uncertainties no dependence of the derivatives on the regularization has been observed. As the figure shows the derivatives are sensibly larger for $a_\mu^{\rm HVP}(s)$ than for $a_\mu^{\rm HVP}(c)$. The typical size of the light sea-quark mass derivative is for the strange HVP $|\partial_\ell^{\rm sea} a_\mu^{\rm HVP}(s)| \sim$ 0.2–0.3 MeV^{-1} while it is of about $|\partial_\ell^{\rm sea} a_\mu^{\rm HVP}(c)| \sim$ 0–0.015 MeV^{-1} for the charm HVP. Considering that the largest light sea-quark mistuning is $\Delta \bar{m}_\ell \sim -0.16$ MeV, the corresponding corrections to the strange HVP, $a_\mu^{\rm HVP}(s)$, turn out to be smaller than 0.1% (which is just slightly smaller than our statistical errors on $a_\mu^{\rm HVP}(s)$ at fixed β), and

[9]The valence-quark mass derivative $\partial_{\rm cr}^{\rm val}$ contribution to both terms in the numerator and denominator of Eq. (D3), which we estimated on the cB211.072.64 ensemble, turns out to be negligible within errors with respect to the sea-quark contribution, and has been neglected.

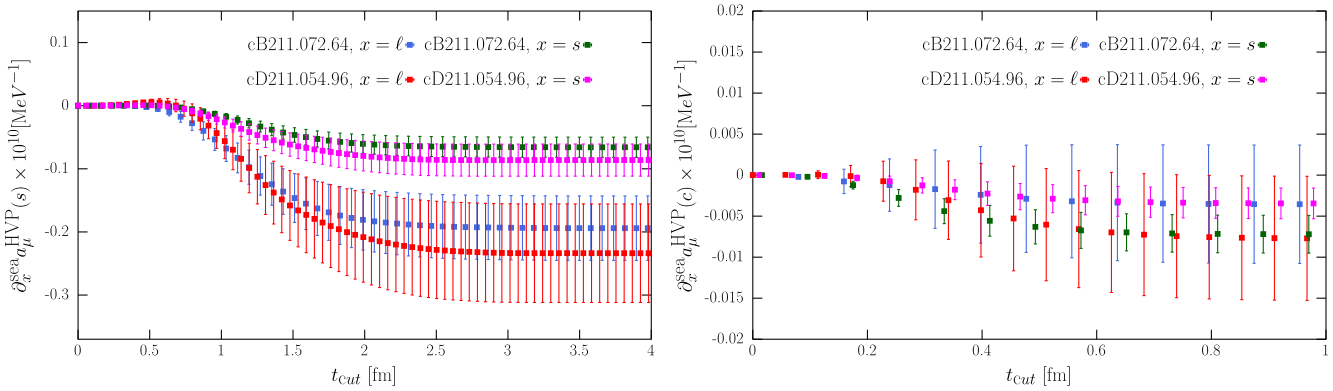

FIG. 17. The light and strange sea-quark mass derivatives of $a_\mu^{\rm HVP}(s)$ (left) and of $a_\mu^{\rm HVP}(c)$, as a function of the upper limit $t_{\rm cut}/a$ on the sum in Eq. (D4), as obtained on the cB211.072.64 and cD211.054.96 ensembles.

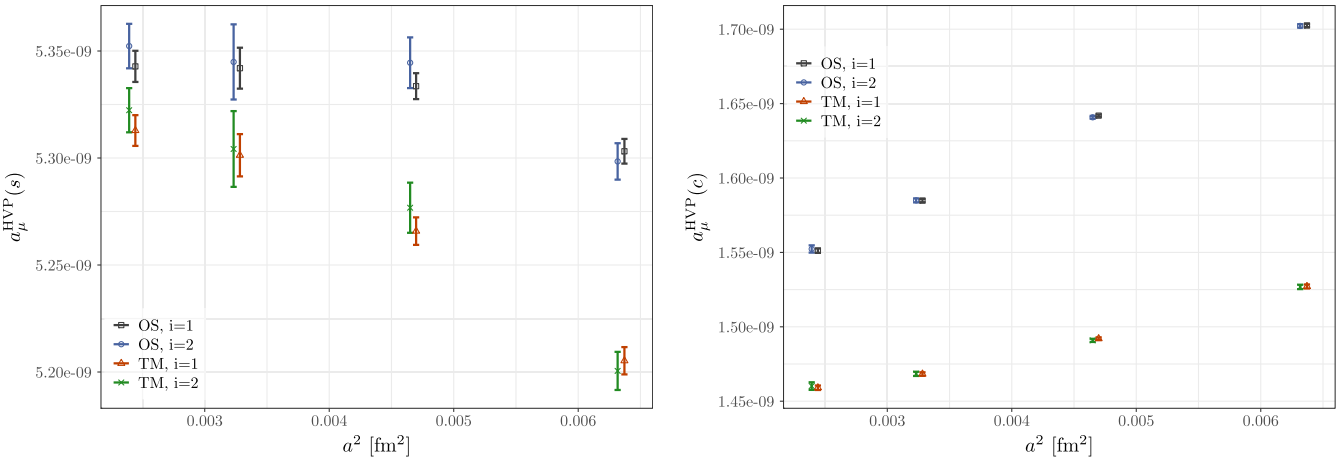

FIG. 18. Comparison between the values of $a_\mu^{\rm HVP}(s)$ (left) and $a_\mu^{\rm HVP}(c)$ (right) obtained before (black for the OS and red for the TM regularization) and after (blue for the OS and green for the TM regularization) applying the corrections due to the mistuning of sea-quark masses and critical mass.

completely negligible for $a_\mu^{\rm HVP}(c)$. The corrections due to the fine-tuning of the critical mass are of a similar magnitude to those resulting from light sea-quark mass mistuning effects.

Concerning the strange sea-quark mass derivatives, they are of order $|\partial_s^{\rm sea} a_\mu^{\rm HVP}(s)| \sim 0.05$–$0.1$ MeV^{-1} and $|\partial_c^{\rm sea} a_\mu^{\rm HVP}(s)| \sim 0.005$–$0.01$ MeV^{-1}. The largest strange sea-quark mass mistuning is $\Delta\bar{m}_s \sim -1.7$ MeV. For the charm HVP, $a_\mu^{\rm HVP}(c)$, the size of this correction is still below (on some ensembles however comparable to) our statistical uncertainties. For the strange HVP, $a_\mu^{\rm HVP}(s)$, however, this mistuning correction is larger than (on some ensembles, up to twice the size of) our statistical uncertainties in $a_\mu^{\rm HVP}(s)$. After accounting also for the charm sea-quark mass mistuning effect, which is estimated using Eq. (D2), the errors on $a_\mu^{\rm HVP}(s)$, as well as on $a_\mu^{\rm HVP,W}(s)$, turn out to be increased. This error increase almost completely offsets the improvement in the intermediate strange window resulting from the addition of a new lattice spacing ensemble (cE211.044.112) and the use of a larger statistics in this calculation as compared to our previous results in Ref. [22]. In Fig. 18 we show, for each β, the comparison between the values of $a_\mu^{\rm HVP}(s)$ and $a_\mu^{\rm HVP}(c)$ obtained before and after applying the corrections due to the mistuning of sea-quark masses and critical mass.

We conclude this section with a comment on the corrections to the scale-invariant RCs Z_V and Z_A (which enter the determination of the strange and charm HVP), due to sea-quark mass and critical mass mistuning effects. For these two quantities the corrections turned out to be extremely tiny, reaching at most, on the coarser ensembles, the level of 0.005–0.01%. For Z_V, which has an astonishing precision $< 0.002\%$, the correction is however larger than the statistical uncertainty. The central

values and errors of Z_V and Z_A, that we provide in Appendix E, are inclusive of the corrections due to mistuning effects.

APPENDIX E: HADRONIC DETERMINATION OF Z_V AND Z_A

In order to reach a high precision determination of the two scale-invariant RCs Z_V and Z_A we employ the hadronic method, already adopted in Ref. [22], based on the Ward identity (WI) and universality of renormalized correlation functions, combined with a high statistics determination of the relevant bare correlators. This allows us to obtain on the ensembles of Table I, after correcting for sea-quark mass and critical mass mistuning effects (see Appendix D), an accuracy of $\simeq 0.03\%$ for Z_A and of $\simeq 0.01\%$ for Z_V, thus reaching the desired accuracy. We collect in Table III the values of Z_A and Z_V used in this work for each of the ETMC ensembles of Table I.

TABLE III. The values of Z_V and Z_A used in this work for each of the ETMC ensembles of Table I, determined by employing the WI-based hadronic method described in Appendix B of Ref. [22].

ensemble	Z_V	Z_A
B64	0.706354(54)	0.74296(19)
B96	0.706406(52)	0.74261(19)
C80	0.725440(33)	0.75814(13)
C112	0.725458(31)	0.75824(15)
D96	0.744132(31)	0.77367(10)
E112	0.758238(18)	0.78548(9)

[1] Muon $g-2$ Collaboration, Measurement of the positive muon anomalous magnetic moment to 0.46 ppm, Phys. Rev. Lett. **126**, 141801 (2021).

[2] M. Abe *et al.*, A new approach for measuring the muon anomalous magnetic moment and electric dipole moment, Prog. Theor. Exp. Phys. **2019**, 053C02 (2019).

[3] Muon $g-2$ Collaboration, Magnetic-field measurement and analysis for the muon $g-2$ experiment at Fermilab, Phys. Rev. A **103**, 042208 (2021).

[4] Muon $g-2$ Collaboration, Beam dynamics corrections to the Run-1 measurement of the muon anomalous magnetic moment at Fermilab, Phys. Rev. Accel. Beams **24**, 044002 (2021).

[5] Muon $g-2$ Collaboration, Measurement of the anomalous precession frequency of the muon in the Fermilab muon $g-2$ experiment, Phys. Rev. D **103**, 072002 (2021).

[6] Muon $g-2$ Collaboration, Final report of the muon E821 anomalous magnetic moment measurement at BNL, Phys. Rev. D **73**, 072003 (2006).

[7] Muon $g-2$ Collaboration, Measurement of the positive muon anomalous magnetic moment to 0.20 ppm, Phys. Rev. Lett. **131**, 161802 (2023).

[8] T. Aoyama *et al.*, The anomalous magnetic moment of the muon in the standard model, Phys. Rep. **887**, 1 (2020).

[9] M. Davier, A. Hoecker, B. Malaescu, and Z. Zhang, A new evaluation of the hadronic vacuum polarisation contributions to the muon anomalous magnetic moment and to $\boldsymbol{\alpha(m_Z^2)}$, Eur. Phys. J. C **80**, 241 (2020).

[10] A. Keshavarzi, D. Nomura, and T. Teubner, $g-2$ of charged leptons, $\alpha(M_Z^2)$, and the hyperfine splitting of muonium, Phys. Rev. D **101**, 014029 (2020).

[11] CMD-3 Collaboration, Measurement of the $e^+e^- \to \pi^+\pi^-$ cross section from threshold to 1.2 GeV with the CMD-3 detector, Phys. Rev. D **109**, 112002 (2024).

[12] CMD-2 Collaboration, High-statistics measurement of the pion form factor in the rho-meson energy range with the CMD-2 detector, Phys. Lett. B **648**, 28 (2007).

[13] G. Abbiendi *et al.*, Mini-proceedings of the STRONG2020 virtual workshop on "space-like and time-like determination of the hadronic leading order contribution to the muon $g-2$", arXiv:2201.12102.

[14] *BABAR* Collaboration, Measurement of additional radiation in the initial-state-radiation processes $e^+e^- \to \mu^+\mu^-\gamma$ and $e^+e^- \to \pi^+\pi^-\gamma$ at *BABAR*, Phys. Rev. D **108**, L111103 (2023).

[15] M. Davier, A. Hoecker, A.-M. Lutz, B. Malaescu, and Z. Zhang, Tensions in $e^+e^- \to \pi^+\pi^-(\gamma)$ measurements: The new landscape of data-driven hadronic vacuum polarization predictions for the muon $g-2$, Eur. Phys. J. C **84**, 721 (2024).

[16] Extended Twisted Mass Collaboration (ETMC) Collaboration, Probing the energy-smeared R ratio using lattice QCD, Phys. Rev. Lett. **130**, 241901 (2023).

[17] S. Borsanyi *et al.*, Leading hadronic contribution to the muon magnetic moment from lattice QCD, Nature (London) **593**, 51 (2021).

[18] A. Boccaletti *et al.*, High precision calculation of the hadronic vacuum polarisation contribution to the muon anomaly.

[19] D. Djukanovic, G. von Hippel, S. Kuberski, H. B. Meyer, N. Miller, K. Ottnad *et al.*, The hadronic vacuum polarization contribution to the muon $g-2$ at long distances, arXiv:2411.07969.

[20] RBC and UKQCD Collaborations, The long-distance window of the hadronic vacuum polarization for the muon g-2, arXiv:2410.20590.

[21] RBC and UKQCD Collaborations, Calculation of the hadronic vacuum polarization contribution to the muon anomalous magnetic moment, Phys. Rev. Lett. **121**, 022003 (2018).

[22] Extended Twisted Mass Collaboration, Lattice calculation of the short and intermediate time-distance hadronic vacuum polarization contributions to the muon magnetic moment using twisted-mass fermions, Phys. Rev. D **107**, 074506 (2023).

[23] C. Alexandrou *et al.*, Simulating twisted mass fermions at physical light, strange and charm quark masses, Phys. Rev. D **98**, 054518 (2018).

[24] Extended Twisted Mass Collaboration, Quark masses and decay constants in $N_f = 2 + 1 + 1$ isoQCD with Wilson clover twisted mass fermions, Proc. Sci. LATTICE2019 (**2020**) 181 [arXiv:2001.09116].

[25] Extended Twisted Mass Collaboration, Ratio of kaon and pion leptonic decay constants with Nf $= 2 + 1 + 1$ Wilson-clover twisted-mass fermions, Phys. Rev. D **104**, 074520 (2021).

[26] J. Finkenrath *et al.*, Twisted mass gauge ensembles at physical values of the light, strange and charm quark masses, Proc. Sci. LATTICE2021 (**2022**) 284 [arXiv:2201.02551].

[27] *Workshop on Converging on QCD+QED Prescriptions* (Higgs Center for Theoretical Physics, Edinburgh, UK, 2024), https://indico.ph.ed.ac.uk/event/257/.

[28] Flavour Lattice Averaging Group (FLAG) Collaboration, FLAG review 2024, arXiv:2411.04268.

[29] D. Giusti, V. Lubicz, G. Martinelli, F. Sanfilippo, and S. Simula, Strange and charm HVP contributions to the muon $(g-2)$ including QED corrections with twisted-mass fermions, J. High Energy Phys. 10 (2017) 157.

[30] D. Giusti, F. Sanfilippo, and S. Simula, Light-quark contribution to the leading hadronic vacuum polarization term of the muon $g-2$ from twisted-mass fermions, Phys. Rev. D **98**, 114504 (2018).

[31] D. Giusti, V. Lubicz, G. Martinelli, F. Sanfilippo, and S. Simula, Electromagnetic and strong isospin-breaking corrections to the muon $g-2$ from lattice QCD + QED, Phys. Rev. D **99**, 114502 (2019).

[32] D. Bernecker and H. B. Meyer, Vector correlators in lattice QCD: Methods and applications, Eur. Phys. J. A **47**, 148 (2011).

[33] M. Garofalo *et al.*, Status of the ETMC calculation of a_μ^{HVP} in isoQCD, in *Talk given at the 41st International Symposium on Lattice Field Theory* (2024).

[34] S. Bacchio, A. Evangelista, R. Frezzotti, G. Gagliardi, M. Garofalo, N. Kalntis *et al.*, Valence leading isospin breaking contributions to $a_\mu^{\mathrm{HVP-LO}}$, arXiv:2501.19350.

[35] R. V. Harlander and M. Steinhauser, RHAD: A program for the evaluation of the hadronic R ratio in the perturbative regime of QCD, Comput. Phys. Commun. **153**, 244 (2003).

[36] European Twisted Mass Collaboration, Up, down, strange and charm quark masses with $\mathrm{N}_f = 2 + 1 + 1$ twisted mass lattice QCD, Nucl. Phys. **B887**, 19 (2014).

[37] E. T. Neil and J. W. Sitison, Improved information criteria for Bayesian model averaging in lattice field theory, Phys. Rev. D **109**, 014510 (2024).

[38] H. Akaike, A new look at the statistical model identification, IEEE Trans. Autom. Control **19**, 716 (1974).

[39] S. Kuberski, M. Cè, G. von Hippel, H. B. Meyer, K. Ottnad, A. Risch, and H. Wittig, Hadronic vacuum polarization in the muon g −2: The short-distance contribution from lattice QCD, J. High Energy Phys. 03 (2024) 172.

[40] χQCD Collaboration, Muon g-2 with overlap valence fermion, Phys. Rev. D **107**, 034513 (2023).

[41] M. Cè *et al.*, Window observable for the hadronic vacuum polarization contribution to the muon g-2 from lattice QCD, Phys. Rev. D **106**, 114502 (2022).

[42] C. Lehner and A. S. Meyer, Consistency of hadronic vacuum polarization between lattice QCD and the R-ratio, Phys. Rev. D **101**, 074515 (2020).

[43] PACS Collaboration, Hadronic vacuum polarization contribution to the muon $g-2$ with $2+1$ flavor lattice QCD on a larger than $(10\ \mathrm{fm})^4$ lattice at the physical point, Phys. Rev. D **100**, 034517 (2019).

[44] A. Gérardin, M. Cè, G. von Hippel, B. Hörz, H. B. Meyer, D. Mohler *et al.*, The leading hadronic contribution to $(g-2)_\mu$ from lattice QCD with $N_{\mathrm{f}} = 2 + 1$ flavours of $\mathrm{O}(a)$ improved Wilson quarks, Phys. Rev. D **100**, 014510 (2019).

[45] Budapest-Marseille-Wuppertal Collaboration, Hadronic vacuum polarization contribution to the anomalous magnetic moments of leptons from first principles, Phys. Rev. Lett. **121**, 022002 (2018).

[46] M. Della Morte, A. Francis, V. Gülpers, G. Herdoíza, G. von Hippel, H. Horch, B. Jäger, H. B. Meyer, A. Nyffeler, and H. Wittig, The hadronic vacuum polarization contribution to the muon $g-2$ from lattice QCD, J. High Energy Phys. 10 (2017) 020.

[47] HPQCD Collaboration, Strange and charm quark contributions to the anomalous magnetic moment of the muon, Phys. Rev. D **89**, 114501 (2014).

[48] Fermilab Lattice, HPQCD, and MILC Collaborations, Hadronic vacuum polarization for the muon $g-2$ from lattice QCD: Complete short and intermediate windows, arXiv:2411.09656.

[49] D. Hatton, C. T. H. Davies, B. Galloway, J. Koponen, G. P. Lepage, and A. T. Lytle (HPQCD collaboration), Charmonium properties from lattice $QCD + QED$: Hyperfine splitting, J/ψ leptonic width, charm quark mass, and a_μ^c, Phys. Rev. D **102**, 054511 (2020).

[50] RM123 Collaboration, Leading isospin breaking effects on the lattice, Phys. Rev. D **87**, 114505 (2013).

[51] K. Jansen and C. Urbach, tmLQCD: A program suite to simulate Wilson twisted mass lattice QCD, Comput. Phys. Commun. **180**, 2717 (2009).

[52] A. Abdel-Rehim, F. Burger, A. Deuzeman, K. Jansen, B. Kostrzewa, L. Scorzato *et al.*, Recent developments in the tmLQCD software suite, Proc. Sci. LATTICE2013 (**2014**) 414 [arXiv:1311.5495].

[53] A. Deuzeman, K. Jansen, B. Kostrzewa, and C. Urbach, Experiences with OpenMP in tmLQCD, Proc. Sci. LATTICE2013 (**2014**) 416 [arXiv:1311.4521].

[54] ETM Collaboration, Twisted mass ensemble generation on GPU machines, Proc. Sci. LATTICE2022 (**2023**) 340 [arXiv:2212.06635].

[55] ETM Collaboration, Lemon: An MPI parallel I/O library for data encapsulation using LIME, Comput. Phys. Commun. **183**, 1321 (2012).

[56] A. Frommer, K. Kahl, S. Krieg, B. Leder, and M. Rottmann, Adaptive aggregation-based domain decomposition multigrid for the lattice Wilson–Dirac operator, SIAM J. Sci. Comput. **36**, A1581 (2014).

[57] C. Alexandrou, S. Bacchio, J. Finkenrath, A. Frommer, K. Kahl, and M. Rottmann, Adaptive aggregation-based

domain decomposition multigrid for twisted mass fermions, Phys. Rev. D **94**, 114509 (2016).
[58] S. Bacchio, C. Alexandrou, and J. Finkerath, Multigrid accelerated simulations for twisted mass fermions, EPJ Web Conf. **175**, 02002 (2018).
[59] C. Alexandrou, S. Bacchio, and J. Finkenrath, Multigrid approach in shifted linear systems for the non-degenerated twisted mass operator, Comput. Phys. Commun. **236**, 51 (2019).
[60] B. Joó, D. D. Kalamkar, T. Kurth, K. Vaidyanathan, and A. Walden, Optimizing Wilson-Dirac operator and linear solvers for intel® KNL, in *High Performance Computing*, edited by M. Taufer, B. Mohr, and J. M. Kunkel (Springer International Publishing, Cham, 2016), pp. 415–427.
[61] M. Schröck, S. Simula, and A. Strelchenko, Accelerating twisted mass LQCD with QPhiX, Proc. Sci. LATTICE2015 (**2016**) 030 [arXiv:1510.08879].
[62] M. A. Clark, R. Babich, K. Barros, R. C. Brower, and C. Rebbi, Solving lattice QCD systems of equations using mixed precision solvers on GPUs, Comput. Phys. Commun. **181**, 1517 (2010).
[63] R. Babich, M. A. Clark, B. Joo, G. Shi, R. C. Brower, and S. Gottlieb, Scaling lattice QCD beyond 100 GPUs, in *SC11 International Conference for High Performance Computing, Networking, Storage and Analysis Seattle, Washington, 2011* (2011), arXiv:1109.2935.
[64] M. A. Clark, B. Joó, A. Strelchenko, M. Cheng, A. Gambhir, and R. C. Brower, Accelerating lattice QCD multigrid on GPUs using fine-grained parallelization, in *SC '16: Proceedings of the International Conference for High Performance Computing, Networking, Storage and Analysis* (2016), pp. 795–806, arXiv:1612.07873.
[65] https://nextgentriggers.web.cern.ch
[66] www.gauss-centre.eu
[67] Jülich Supercomputing Centre, JUWELS: Modular tier-0/1 Supercomputer at the Jülich Supercomputing Centre, J. Large-Scale Res. Facil. **5**, A135 (2019).
[68] Jülich Supercomputing Centre, JUWELS cluster and booster: Exascale Pathfinder with modular supercomputing architecture at Juelich Supercomputing Centre, J. Large-Scale Res. Facil. **7**, A183 (2021).
[69] S. Aoki, R. Frezzotti, and P. Weisz, Computation of the improvement coefficient c_{sw} to one loop with improved gluon actions, Nucl. Phys. **B540**, 501 (1999).
[70] Y. Iwasaki, Renormalization group analysis of lattice theories and improved lattice action: Two-dimensional nonlinear O(N) sigma model, Nucl. Phys. **B258**, 141 (1985).
[71] B. Sheikholeslami and R. Wohlert, Improved continuum limit lattice action for QCD with Wilson fermions, Nucl. Phys. **B259**, 572 (1985).
[72] R. Frezzotti and G. C. Rossi, Chirally improving Wilson fermions. II. Four-quark operators, J. High Energy Phys. 10 (2004) 070.
[73] R. Frezzotti and G. C. Rossi, Chirally improving Wilson fermions. 1. O(a) improvement, J. High Energy Phys. 08 (2004) 007.
[74] R. Frezzotti, G. Martinelli, M. Papinutto, and G. C. Rossi, Reducing cutoff effects in maximally twisted lattice QCD close to the chiral limit, J. High Energy Phys. 04 (2006) 038.
[75] B. Kostrzewa (ETMC Collaboration), Status of the ETMC ensemble generation effort, in Talk Given at the 41st Lattice Conference (University of Liverpool, United Kingdom, 2024), https://conference.ippp.dur.ac.uk/event/1265/contributions/7655/attachments/5599/7311/Poster_Garofalo_Kostrzewa_Lattice_2024_ETMC_simstatus.pdf.
[76] J. Gasser and H. Leutwyler, Chiral perturbation theory to one loop, Ann. Phys. (N.Y.) **158**, 142 (1984).
[77] Extended Twisted Mass Collaboration, Inclusive hadronic decay rate of the τ lepton from lattice QCD: The $\bar{u}s$ flavor channel and the Cabibbo angle, Phys. Rev. Lett. **132**, 261901 (2024).